SEDIMENTOLOGY the journal of the International Association of Sedimentologists IAS

Sedimentology (2024) **71**, 2378–2403 doi: 10.1111/sed.13220

Hourly to weekly variations in halite precipitation from the hypersaline Dead Sea: The role of evaporation, water cooling and freshwater plume stability

ZIV MOR*,†, GIL NOY*,†, HAGGAI EYAL*,†, IDO SIROTA*,‡, ROIE EZRATY*,†, EFRAT MORIN† and NADAV G. LENSKY*,†

**Geological Survey of Israel, 32 Yesha'yahu Leibowitch Street, Jerusalem 9692100, Israel (E-mail: ziv.mor@mail.huji.ac.il) (E-mail: nadavl@gsi.gov.il)*

†The Fredy and Nadine Herrmann Institute of Earth Sciences, The Hebrew University of Jerusalem, Givat Ram, Jerusalem 91904, Israel

‡Section Climate Dynamics and Landscape Evolution, GFZ German Research Centre for Geosciences, Telegrafenberg 14473, Potsdam, Germany

Associate Editor – Ashleigh Hood

ABSTRACT

Thick-bedded halite sequences in the geological record are characterized by lateral variations, reflecting spatiotemporal variations in environmental forcing. Although temporal variations have been examined over seasonal scales or longer durations, there is a paucity of information regarding the dynamics of halite deposition at shorter durations of days and hours. Additionally, the influence of water discharges and surface salinity gradients remains poorly understood. Here, for the first time, *in situ*, hourly to weekly halite accumulation rates were measured on the Dead Sea floor (*ca* 20 m water depth), the only modern deep and hypersaline water body. Novel underwater photography methods were developed to directly observe halite precipitation at the lake floor, coeval with monitoring of the environmental drives, i.e. evaporation, meteorological and limnological conditions. Two fundamental environments were explored: a diluted plume environment arising from spring discharge; and a mixed hypersaline environment. The focus was on deposition during winter when the halite accumulation rate is highest, and the relationship between evaporation and halite accumulation is most straightforward since the water column is vertically uniform. Significant spatial variations in halite accumulation were found between the two environments, along with hourly variations in each environment. In the mixed hypersaline environment, over intra-diurnal timescales, evaporation plays a more significant role in halite precipitation, whereas temperature has a greater impact on seasonal changes. In the diluted plume environment, the stability of the buoyant plume controls the rate of halite deposition; during windstorms, the plume is stirred, with higher surface water salinity and higher rate of halite accumulation. However, under calm winds, the plume is stable, with diluted surface water, and the rate of halite accumulation is a few times lower. Following these new findings, the implications for the interpretation of halite deposits are discussed.

Keywords Dead Sea, evaporation, evaporites, halite deposition, hypersaline lakes, limnogeology.

INTRODUCTION

Thick halite layers were deposited throughout Earth's geological history in perennial, deep and wide hypersaline water bodies (Schmalz, 1969; Lowenstein & Hardie, 1985; Warren, 2010; Roveri *et al.*, 2014a,b; Gvirtzman *et al.*, 2017; Kiro *et al.*, 2017), along with shallow perennial and shallow ephemeral hypersaline environments (Morris & Dickey, 1957; Butler, 1969; Lowenstein & Hardie, 1985; Casas & Lowenstein, 1989; Schubel & Lowenstein, 1997; Goodall *et al.*, 2000; Benison *et al.*, 2007; Lokier, 2012; Bowen *et al.*, 2017). Continuous accumulation of halite layers requires extreme aridity and an overall negative water balance, where evaporation from the surface of the water body is greater than freshwater inflows (Hovorka, 1987; Lowenstein, 1988; Li *et al.*, 1996; Manzi *et al.*, 2012; Kiro *et al.*, 2016; Sirota *et al.*, 2017). These deposits are commonly used in reconstructing palaeo-hydroclimate conditions because the thickness of the halite deposits and their textures are related to net evaporation via mass balance consideration (Anderson, 1982; Li *et al.*, 1996; Manzi *et al.*, 2012; Torfstein *et al.*, 2015; Kiro *et al.*, 2016). Such hydroclimatic reconstructions require a solid understanding of how temporal and spatial variations in hydroclimatic conditions are recorded within the evaporitic sedimentary archive. Significant knowledge has been gained over the years from the study of halite deposition/dissolution in shallow hypersaline environments, which is governed primarily by the water balance (e.g. Lowenstein & Hardie, 1985; Benison & Goldstein, 2000, 2001; Benison *et al.*, 2007; Bowen *et al.*, 2017; Bernau & Bowen, 2021; Bernau *et al.*, 2022). The relation between environmental drivers and halite deposition in deep hypersaline water bodies is more complicated, due to the transport of heat and mass within the water column, as was recently examined by direct observations from the Dead Sea (Arnon *et al.*, 2016; Sirota *et al.*, 2016, 2017, 2018, 2020).

Temporal variations in the hydroclimatic conditions are reflected throughout the bedding of halite sequences, including variations in crystal size, sedimentary structures, the association of detrital materials, cementation and dissolution features (Lowenstein & Hardie, 1985; Benison & Goldstein, 1999; Manzi *et al.*, 2012; Kiro *et al.*, 2016; Palchan *et al.*, 2017; Olson & Lowenstein, 2021; Sirota *et al.*, 2021; Olson *et al.*, 2023). The deposition rate and textures are governed by the degree of halite saturation (Sirota *et al.*, 2017), which is dictated by the rate of change in brine temperature and salinity (Sirota *et al.*, 2016). The solubility of halite is temperature-dependent; thus, the cooling of saturated brine results in supersaturation and halite deposition. In shallow lakes, the effect of cooling/heating on halite deposition/dissolution occurs along the diurnal cycles (Dellwig, 1955; Arthurton, 1973; Roedder, 1982; Roberts & Spencer, 1995), whereas in deep lakes, that have longer thermal response time (Tau *et al.*, 2022), the effect is mainly on the seasonal timescale, resulting in most halite deposition occurring during the winter (Sirota *et al.*, 2016, 2017). Interestingly, evaporation results in increased halite saturation through two processes: increasing the concentration of the brine, and cooling of the brine by utilizing latent heat. Although major variations in evaporation and water temperature are often documented at hourly to seasonal scales (Arnon *et al.*, 2016; Hamdani *et al.*, 2018; Lensky *et al.*, 2018; Mor *et al.*, 2018, 2021; Ezraty *et al.*, 2021), the dynamics of halite deposition on the floor of a deep hypersaline lake have so far been documented only at the seasonal scale, not at sub-seasonal (weeks) to hourly scales. Sub-seasonal timescales are observed in the sedimentary record (Sirota *et al.*, 2021; Brall *et al.*, 2022), but have not been observed yet in modern deep hypersaline lakes, only in shallow hypersaline environments (Lowenstein & Hardie, 1985; Lokier, 2012).

Spatial variations in halite deposits can originate from lateral salinity gradients (Fig. 1), which are recognized as critical in understanding the sedimentary architecture of evaporitic basins (Schmalz, 1969; Roveri *et al.*, 2014a; Flecker *et al.*, 2015; Karakitsios *et al.*, 2017) and the evolution of these basins when they are connected to diluted water masses (Krijgsman & Meijer, 2008). The inflow of less saline water may generate diluted water plumes that spread over the denser hypersaline brine (Mor *et al.*, 2018, 2021). The internal salinity structure of the diluted plumes varies significantly, depending primarily on inflow rates and salinity, wave amplitude (and, in places, tidal amplitude), coastline geometry, ambient currents, properties of the hosting waterbody (temperature, salinity and density differences) and wind stress (Fong, 1998; Fong & Geyer, 2001; Hetland, 2005, 2010; Hetland & Hsu, 2013; Horner-Devine *et al.*, 2015). Fresh inflows are limited in their discharge during dry periods of evaporite deposition, but they still have a local impact on evaporite deposition by reducing brine saturation and the resulting evaporite accumulation

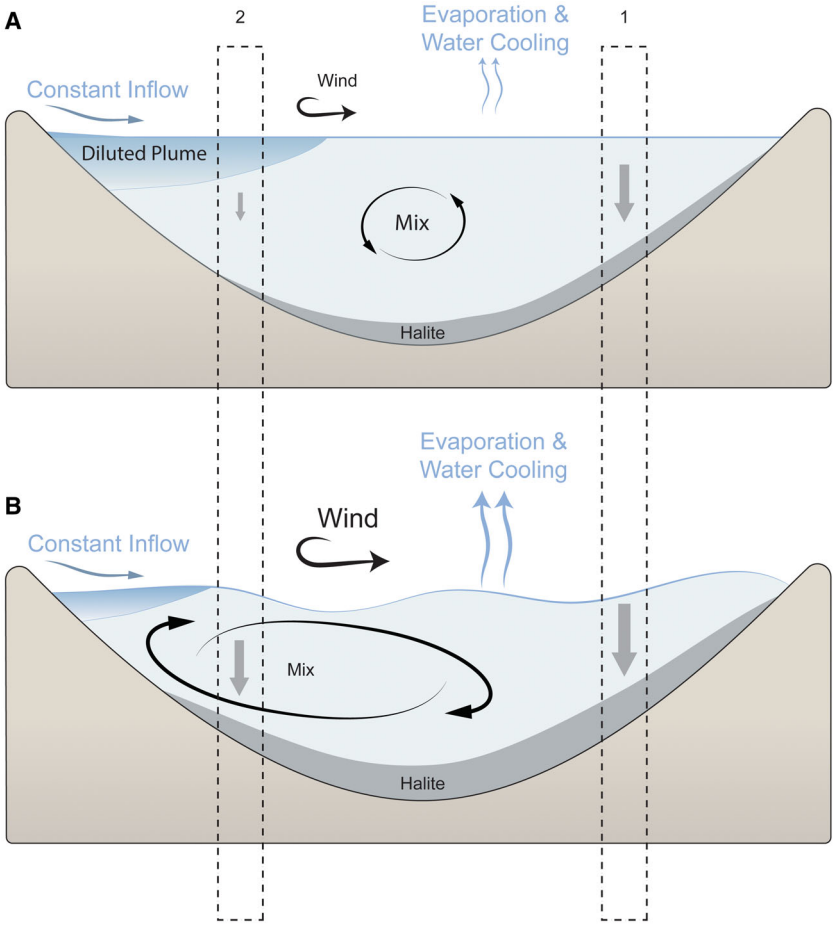

Fig. 1. Schematic illustration of variations in the environmental drivers and the resulting hypothesized halite accumulation. Vertical sections of the lake, which is mostly a mixed hypersaline waterbody, along with local constant freshwater inflow and the resulting diluted plume. Focus is on two different environments (dashed rectangles 1 and 2, for the mixed saturated brine and the diluted plume, respectively). (A) The low intensity of environmental forcing (i.e. evaporation, water cooling and wind speed) resulted in a low rate of halite accumulation in the mixed saturated brine (location 1) and a stable diluted plume with lower halite precipitation (location 2). (B) High intensity of environmental forcing resulted in a higher rate of halite accumulation in the mixed saturated brine (location 1), whereas the destabilized plume resulted in a much higher accumulation rate compared to the stable diluted plume due to higher wind stress (location 2). The depth scale is over tens of metres.

(Yoshimura *et al.*, 2016; Karakitsios *et al.*, 2017; Sirota *et al.*, 2020). Although major variations in evaporation, water temperature and salinity have been documented in diluted plumes (Mor *et al.*, 2018, 2021; Sirota *et al.*, 2020), their influence on the dynamics of halite deposition has not been examined.

This research explores for the first time the relationship between hourly active halite precipitation and hourly environmental drivers in the closest modern analogue of deep hypersaline environments, the Dead Sea (see details in the section on *Dead Sea regional setting*). Two different environments are explored: (i) the mixed halite-saturated region that characterizes most of the lake (Fig. 1A and B, location 1); and (ii) a diluted plume environment arising from spring discharge (Fig. 1A and B, location 2). These environments are located in the same hypersaline basin, experiencing the same overall negative water balance and level decline, which lead to halite precipitation. Wintertime sedimentation was studied, because this period exhibits the highest deposition rates and the most straightforward relationship between evaporation and halite accumulation due to vertical mixing of the water column. It is hypothesized that halite accumulation varies according to environmental drivers,

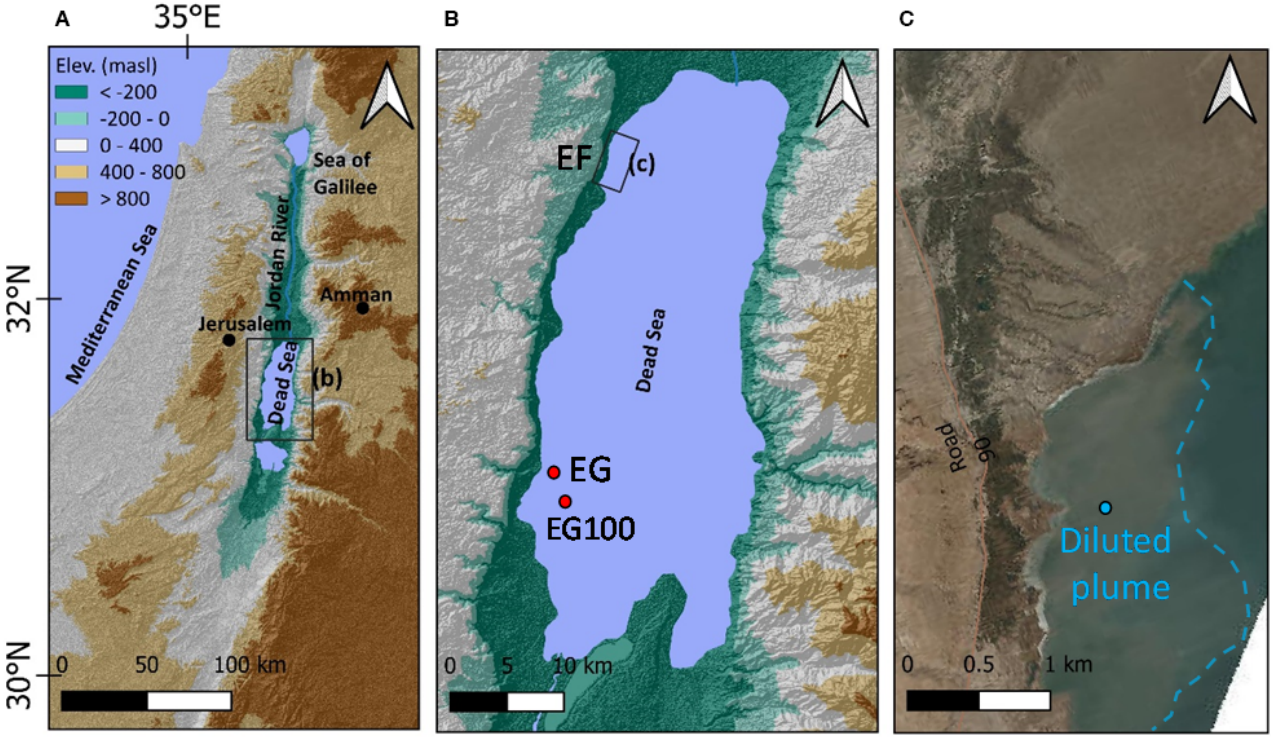

Fig. 2. Dead Sea location maps. Regional map (A), Dead Sea topography (B) with the studied areas indicated: EG (Ein Gedi) and the research buoy EG100 represent the mixed saturated brine far from the dilution effect, and EF (Ein Feshkha springs) represents the diluted region of the lake due to freshwater inflow, as shown in the close-up aerial photograph (C). The cyan dot represents the location of the research buoy located in the area affected by the diluted plume. The plume front is identified by the turbidity of the surface water (represented as a dashed cyan line); this front migrates with changes in the external conditions (see Fig. 1). Note that the EG offshore station (EG100) well-represented the onshore station (see Lensky *et al.*, 2017 for more details). In (A) and (B) Digital elevation model (DEM) and hill shade of 30 m pixel^{-1} resolution was obtained from the Geological Survey of Israel, and in (C) an aerial photograph was obtained from https://www.govmap.gov.il/.

including evaporation, water cooling and freshwater plume stability, resulting in sedimentary spatiotemporal variations (Fig. 1). This study aims to: (i) characterize the hourly and weekly accumulation of halite in a mixed hypersaline environment and in a diluted plume environment arising from spring discharge; (ii) explore the relations between the governing environmental drivers and halite accumulation; and (iii) provide implications for interpreting the rock record.

DEAD SEA REGIONAL SETTING

The Dead Sea is a hypersaline terminal lake located at the lowermost land surface on Earth in a subsiding pull-apart basin along the Dead Sea transform fault (Garfunkel, 1981) (Fig. 2A). The lake level is currently (2024) –439 m relative to sea level (asl) (Israel Hydrological Service, 2024). The lake's surface area is approximately 600 km^2 and the deepest basin floor is at a water depth of approximately 280 m (Sade *et al.*, 2014) (Fig. 2B). The Dead Sea level is declining rapidly, at a rate of >1 m year^{-1}, in response to the diversion of inflow water and continuous evaporation from the lake surface, i.e. negative water balance (Lensky *et al.*, 2005; Lensky & Dente, 2015).

Evaporation

The annual rate of evaporation from the Dead Sea, based on two years of direct eddy covariance measurements, is 1.13 ± 0.13 m year^{-1} (Hamdani *et al.*, 2018). At the hourly timescale, there is a good temporal correlation between the evaporation rate and wind speed (Lensky *et al.*, 2017; Hamdani *et al.*, 2018; Mor *et al.*, 2018; Ezraty *et al.*, 2021). The seasonal cycle of evaporation is characterized by two peaks (Hamdani

et al., 2018): (i) the summer evaporation peak is related to high radiative forcing; and (ii) the winter evaporation peak stems from the high heat storage of the deep lake, with evaporation driven by high vapour pressure demand and thermal instability, combined with relatively high wind speed during synoptic-scale storms, mostly Mediterranean cyclones (MCs) (e.g. Alpert *et al.*, 1990) and Red Sea troughs during autumn and spring (e.g. Kahana *et al.*, 2002). These synoptic events last up to several days, with distinct microclimate characteristics (i.e. wind speed, humidity and air temperature), resulting in high intraseason and interseason variance of evaporation rates (Hamdani *et al.*, 2018).

Halite precipitation

The decadal lake level decline was associated with an increase in salinity and density of the upper layer (epilimnion) of the Dead Sea; in the early 1980s, the salinity reached the value for halite saturation, and halite started precipitating at a rate of *ca* $0.1\,m\,year^{-1}$ (Steinhorn, 1983; Levy, 1992; Beyth *et al.*, 1993; Gavrieli, 1997; Stiller *et al.*, 1997; Lensky *et al.*, 2005; Sirota *et al.*, 2016, 2017). Concurrently, the density of the epilimnion reached that of the deep water mass (hypolimnion) and, subsequently, the limnologic state of the Dead Sea changed from meromictic (permanent stratification) to holomictic (seasonal thermal stratification). In the holomictic stage, during summer, the lake is stratified with a warmer and saltier stable epilimnion (thermocline depth of *ca* 25 m), whereas during winter, the cooling of surface water leads to vertical mixing of the water column (Steinhorn, 1985; Anati *et al.*, 1987; Anati & Stiller, 1991; Gertman & Hecht, 2002; Arnon *et al.*, 2016).

The degree of halite saturation and deposition rates vary with depth and season according to the temperature and salinity distribution, and the transport of heat and dissolved salt (Arnon *et al.*, 2016; Sirota *et al.*, 2016, 2017, 2020, 2021). The accumulated halite sequences exhibit distinct alternations of summer and winter layers, i.e. varves (Sirota *et al.*, 2017). The process linking evaporation to halite precipitation and accumulation on the lake floor during summer is not straightforward; evaporation takes place on the water surface in the undersaturated epilimnion, and intricately coupled mechanisms involving the diffusive and convective transport of the dissolved salt to the hypolimnion drive halite deposition to the basin floor (Arnon *et al.*, 2016; Sirota *et al.*, 2016, 2017; Ouillon *et al.*, 2019). Summer halite beds in the hypolimnion are composed of bottom growth crystals characterized by rough and coarse crystals and a consolidated halite layer; the coarse crystals actively grow from the bed upward. During winter, when the water column is well-mixed, cooling of the water column results in intensive halite precipitation along the entire water column in response to the high degree of supersaturation of the water column. The deposited halite layer is composed of fine unconsolidated halite crystals, termed cumulates, that nucleate along the water column and then settle to the lake floor. Furthermore, Sirota *et al.* (2021) showed that within a winter cumulate layer, thin laminae of crystals slightly coarser than the typical fine cumulates exist, and in places are associated with mud. These fine laminations may reflect a short-term lower degree of halite supersaturation (Sirota *et al.*, 2017). Therefore, variations in cumulate halite layers can potentially shed light on hourly to weekly hydroclimatic variations.

Freshwater inflows

The major sources of freshwater discharge into the Dead Sea are mainly from the Jordan River (presently discharging *ca* $100 \times 10^6\,m^3\,year^{-1}$) and from the Ein Feshkha springs system (EF) (presently discharging *ca* $70 \times 10^6\,m^3\,year^{-1}$) (Fig. 2C), both located in the northern Dead Sea (Lensky *et al.*, 2005). These point sources of freshwater inflows form a diluted plume that spreads laterally over the Dead Sea and can reach up to a 90% dilution (density of *ca* $1020\,kg\,m^{-3}$ versus *ca* $1243\,kg\,m^{-3}$ and quasi-salinity of *ca* $20\,kg\,m^{-3}$ versus *ca* $243\,kg\,m^{-3}$) (Mor *et al.*, 2018, 2021). The distinct diluted area modifies the water–air interactions (Mor *et al.*, 2018), thermohaline stratification (Sirota *et al.*, 2020; Mor *et al.*, 2021) and vertical transport of dissolved salt (Sirota *et al.*, 2020). The dynamics of the diluted plume over the Dead Sea are primarily controlled by vertical water column mixing as a result of wind–wave action; high wind speed ($>4\,m\,s^{-1}$) results in the mixing of the diluted plume and reduces the extent of the diluted surface water (Mor *et al.*, 2018, 2021). Thus, wind–wave action and the degree of dilution are hypothesized to modify the rate of halite precipitation under the plume.

Geological observations of the spatial extent of the early Holocene halite deposits in the subsurface show that they are absent from the northern part of the western Dead Sea coasts (Abelson *et al.*, 2006, 2017). This northern limit of early Holocene halite layers has been related to

variations in halite deposition following salinity gradients across the water body (Sirota *et al.*, 2020). During exceptionally wet winters with high stream discharges, lake levels rise, and the entire surface water becomes diluted, preventing halite accumulation throughout the lake (Beyth *et al.*, 1993; Sirota *et al.*, 2021). Additionally, halite dissolves from the shallow marginal parts of the lake (Beyth *et al.*, 1993; Sirota *et al.*, 2021). The findings from these previous studies imply the potential effect of dilution versus mixed supersaturated brine on the shorter timescales of halite deposition in the Dead Sea.

OBSERVATIONAL SETUP, METHODS AND ANALYSIS

The active accumulated halite on the lake floor was measured using novel underwater photography methods, simultaneously with measurements of the environmental forcing, evaporation rate and water cooling, in hourly to weekly increments. Combining these observations allows for examination of the relationship between halite accumulation and environmental drivers on an hourly scale. Measurements were carried out at two different environments on the west coast of the Dead Sea, approximately 30 km apart (Fig. 2): (i) mixed supersaturated brine, measured at Ein Gedi (EG) far away from the freshwater inflow effect; and (ii) a diluted plume fed by the Dead Sea's largest spring, the Ein Feshkha springs (EF).

Halite precipitation on the lake floor

To observe and measure the accumulated halite cover on the lake floor, two novel techniques were developed and employed: (i) an underwater time-lapse camera for high temporal documentation (20 min) (Fig. 3A and B); and (ii) for longer periods (>11 days), remotely operated vehicle (ROV) observations of accumulation on concrete blocks positioned on the lake floor (Fig. 3A and C). Both are placed in a water depth of *ca* 20 m, in relatively close proximity (tens of metres apart).

Underwater time-lapse camera – hourly and daily resolution

Hourly measurements of halite cover were obtained using an underwater time-lapse camera (TLC) for *ca* 11 days in each location during the winter of 2022 (13–25 January 2022 and 2–13 February 2022, in Ein Gedi and Ein Feshkha springs system, respectively, Fig. 4). The underwater time-lapse camera (Astral-Subsea Marine Robotics, Michmoret, Israel; Figs 3B and 5) consists of a high-performance mirrorless digital camera (XT3, Fujifilm Corporation, Tokyo, Japan) with a 60 mm lens (XF 80 mm, Fujifilm Corporation) that captures high-resolution pictures (6240 × 4160 pixels). The aperture key was set to f/16 to gain a larger depth of field. The underwater time-lapse camera apparatus consists of: (i) a stainless-steel frame; (ii) a camera that is placed within a Plexiglas waterproof housing rated to a 50 m depth; (iii) a lithium battery (11.1 V/91 Ah) that is placed in a cylindrical Delrin housing; (iv) an LED light that is bright enough (1500 lumen) to reduce the natural background light, which during daytime introduces 'greenish' colours; and (v) a control unit. The underwater time-lapse camera was programmed to take pictures in 20 min intervals; each picture was taken after the light was switched on with automatic focus. The object is a horizontal plate (sediment trap), 20 × 20 cm, with a vertical ruler at the centre of the plate, with millimetric marks.

In situ halite accumulation thickness identified at a resolution of 0.25 mm, which is due to the collective limitations of the pixel resolution (0.05 mm), ruler resolution and the most significant factor – the smoothness of the accumulated layers, i.e. the actively depositing fine-grained halite forms cumulate layers that are not perfectly planar over the field of view of the underwater time-lapse camera. The time series of halite thickness consists of 0.25 mm thickness steps as frames had to be skipped until another interval of 0.25 mm was accumulated. The halite deposition rate was calculated as the time derivative of the halite accumulation time series. Furthermore, the set of pictures was used to estimate accumulated halite crystal size (±0.05 mm), with a time interval of *ca* 6 h for the size distribution. In each picture, the size of *ca* five crystals that were close enough to the millimetric ruler (up to *ca* 50 mm) and were fully illuminated (reflected) by the underwater time-lapse camera light was estimated. The estimation of halite crystal size is illustrated in Fig. S1.

Remotely operated vehicle observations of halite accumulation over a concrete block – weekly resolution

Weekly interval measurements of halite accumulation over a concrete block were performed using a remotely operated vehicle (ROV; Revolution, Deep Trekker Inc., Kitchener, ON, Canada). The ROV is equipped with a 720p video (1280 × 720

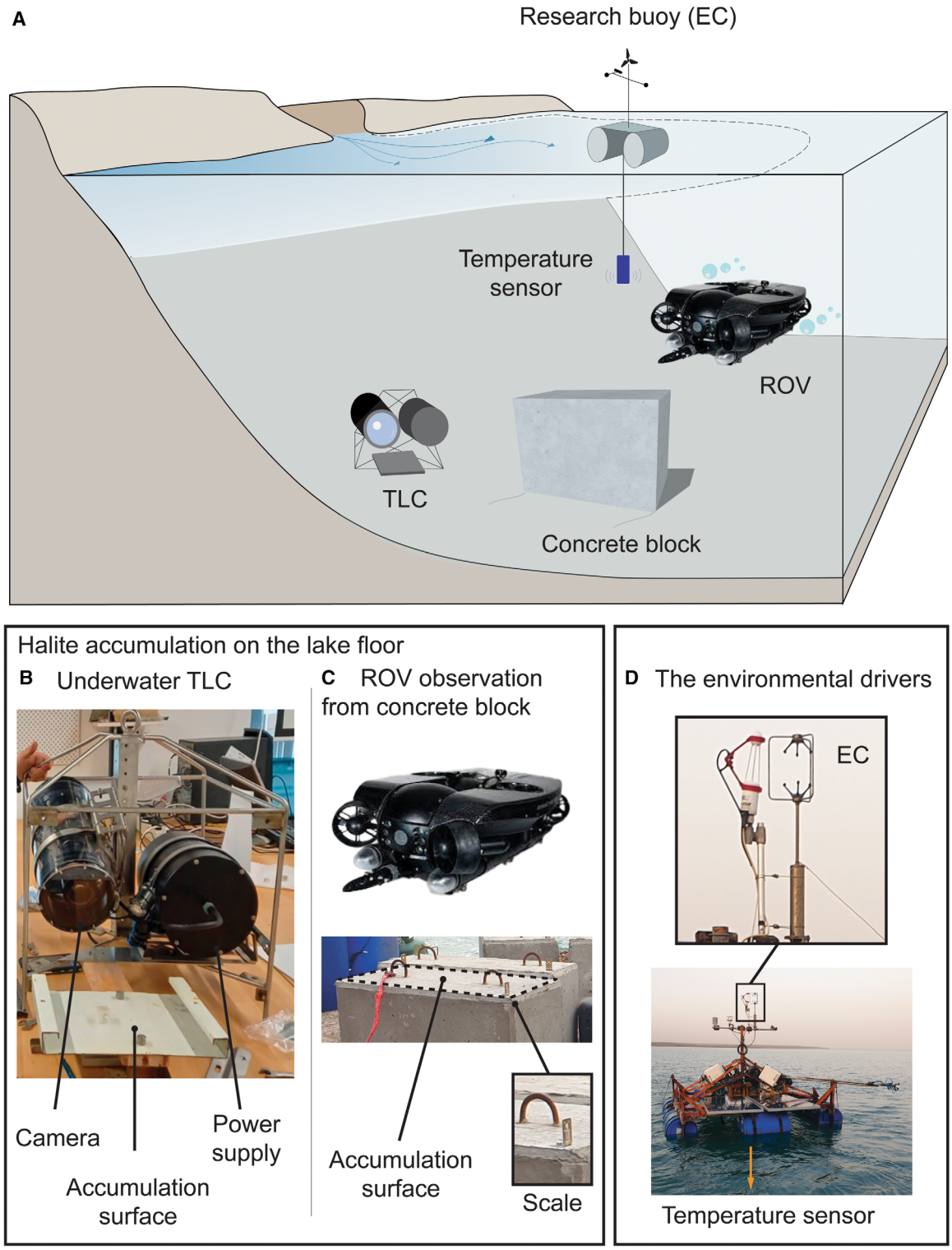

Fig. 3. Observational setup and monitoring equipment. (A) The observational setup in the two study sites (diluted plume shown, but an identical setup was used for the mixed supersaturated brine); determination of the halite accumulation rate by (B) the underwater time-lapse camera (TLC) imagery and (C) a concrete block that was deployed on the lake floor as a time marker and was monitored using a remotely operated vehicle (ROV). (D) A research buoy equipped with an eddy covariance system for measuring the evaporation rate; a meteorology station and a water temperature profiler.

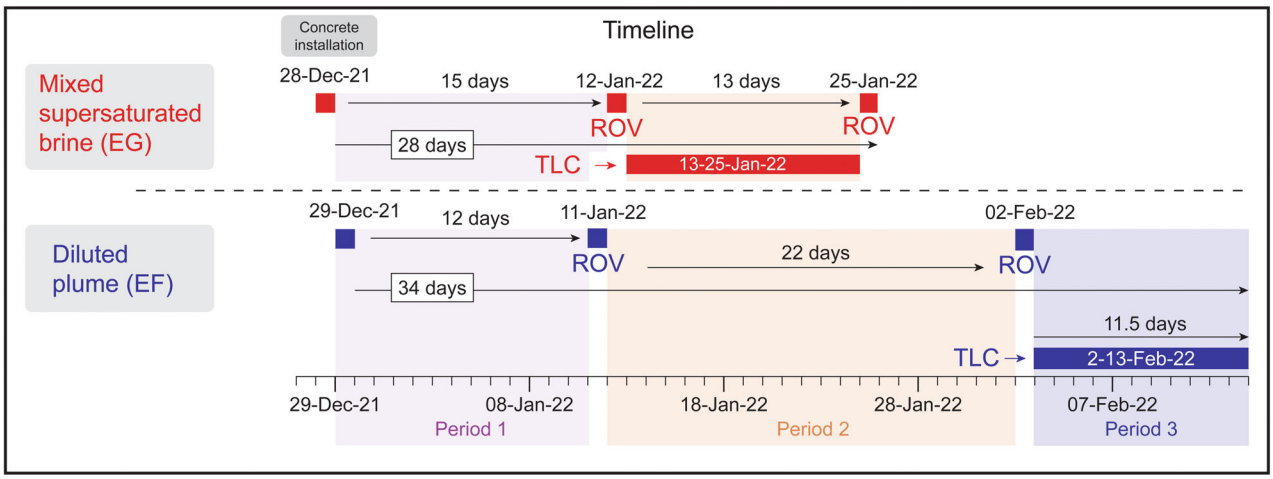

Fig. 4. Timeline of the observations conducted during winter 2021 to 2022 surveys.

Fig. 5. The time-lapse camera device, following ten days of deployment in the mixed supersaturated brine site. The camera is covered by fine halite crystals that settle from the water column (i.e. cumulates). (A) The camera housing with the flat transparent port, (B) the flashlight and (C) the battery and controller unit in the cylindrical housing.

pixels), powerful LED lights (total of 11 800 lumens), a laser scale, multibeam sonar (Oculus, Blueprint Subsea, Ulverston, UK) and an arm manipulator. Placement of 750 kg concrete blocks (50 cm high, 50 cm wide and 100 cm long) on the lake floor occurred on 28 and 29 December 2021 in Ein Gedi and Ein Feshkha, respectively (Fig. 4). The blocks were placed at a water depth of *ca*

20 m, which is *ca* 200 m offshore of the Ein Feshkha springs and from the Ein Gedi shore. An L-shaped iron angle (34 mm × 65 mm) was attached to the blocks and was used as a scale for halite accumulation thickness (Fig. 3C). The concrete blocks were tethered to a 200 l plastic barrel with a 5 m rope for easier detection while using the multibeam sonar.

The accumulated halite over the concrete block was measured twice at each environment (Fig. 4). Measurements occurred at Ein Gedi, 15 and 28 days after installation on 12 January 2021 and 25 January 2021, respectively, and at Ein Feshkha, 15 and 35 days after installation on 13 January 2021 and 2 February 2022, respectively. Measuring the accumulated halite thickness involved: (i) navigating with the ROV to the target location; (ii) exposing the L-shaped scale with the ROV arm manipulator; (iii) observing and recording the halite cover from different angles; and (iv) measuring/estimating halite thickness from the highest-quality pictures. The estimated error is on the order of *ca* 2 to 5 mm, and it varies according to image quality, which depends on the photographing angle, distance from the concrete surface and the L-shaped scale, and the accumulated halite uniformity across the concrete surface.

Environmental drivers of halite accumulation

Evaporation and water temperature were measured from an offshore research buoy, in both environments (Fig. 3A and D). The diluted plume research buoy is located *ca* 250 m offshore of the spring outflow at the Ein Feshkha site (Fig. 2C, see more details in Mor *et al.*, 2021), while the mixed supersaturated brine research buoy (EG100) is located *ca* 4.5 km offshore of the Ein Gedi shore (Fig. 2B, see more details in Lensky *et al.*, 2017; Hamdani *et al.*, 2018; Ezraty *et al.*, 2021). It was found that the Ein Gedi offshore station (EG100) well-represented the onshore station, as indicated by the close relation between wind speed, air temperature and humidity (U, Ta and RH) at the two stations (Lensky *et al.*, 2017).

Evaporation was measured using eddy covariance (EC) systems. Each EC system is equipped with a 3D Sonic Anemometer (WindMaster Pro, Gill Instruments, Lymington, UK) and an Open Path CO_2/H_2O Gas Analyser (LI-7500A; LI-COR, Lincoln, NE, USA), sampling at 20 Hz. The 20 Hz raw data were processed and corrected to obtain half-hourly eddy fluxes using EddyPro software (LI-COR). Some invalid flux measurements were obtained due to low-quality data, and these were flagged by EddyPro (the available data accounted for 98% and 96% of the total dataset for Ein Gedi and Ein Feshkha, respectively). The location and design of the research buoys allowed measurement of the fluxes from all wind directions (Ezraty *et al.*, 2021; Mor *et al.*, 2021).

Water temperatures were measured every 10 min using thermistors (CS225-L, Campbell Scientific Inc., Logan, UT, USA; 36XiW, KELLER, Winterthur, Switzerland). These thermistors were hung under buoys at water depths of 15 m and 13 m for Ein Gedi and Ein Feshkha, respectively.

Waves were analysed using water pressure data (PAA 36XiW; KELLER), measured at 4 Hz at a depth of *ca* 10 m on the lake floor, *ca* 6 km north of the Ein Feshkha springs system site (31.737732°, 35.492941°). From the continuous 4 Hz data, differences between maximum and minimum pressure at a 10 min resolution were used as proxies for the wave height. Waves are scaled between 0 to 1, where 1 represents the highest waves. According to measurements taken at this site, the maximum wave height recorded was approximately 4 m (Eyal *et al.*, 2021). For more detailed information on these methods of wave measurement, refer to Eyal *et al.* (2021).

Theoretical relation between evaporation, water cooling and halite accumulation

Presented here is a theoretical model based on mass conservation that predicts halite accumulation rates given the environmental drivers atop a saturated brine. This model is evaluated in the discussion section. The two major governing processes controlling the degree of saturation (*Se*), leading to halite precipitation in nearly saturated brines, are an increase in salinity and a decrease in temperature (Stiller *et al.*, 1997; Sirota *et al.*, 2016). Both of these processes lead to the supersaturation of the brine and, consequently, the nucleation of halite. The cooling and evaporation effects on halite accumulation thickness, denoted as $D_{\mathrm{cool}}[\mathrm{m}]$ and $D_{\mathrm{evap}}[\mathrm{m}]$, respectively, was examined separately. The overall thickness of the halite accumulation layer, denoted as D_{tot}, is the combined result of both cooling and evaporation, expressed as $D_{\mathrm{tot}}[m] = D_{\mathrm{cool}}[\mathrm{m}] + D_{\mathrm{evap}}[\mathrm{m}]$.

The saturated brine density ($\rho\left[\frac{\mathrm{kg}}{\mathrm{m}^3}\right]$), under small density differences ($\frac{\Delta\rho}{\rho} \ll 1$), is assumed to depend linearly on the water temperature (T [K]), salinity concentration as a mass fraction ($S\left[\frac{\mathrm{kg}}{\mathrm{kg}}\right]$) and halite crystal mass fraction ($C\left[\frac{\mathrm{kg}}{\mathrm{kg}}\right]$):

$$\rho\,(T,S,C) = \alpha T + \beta_S S + \beta_C C \tag{1}$$

where $\alpha\left[\frac{\mathrm{kg}}{\mathrm{m^3 K}}\right]$, $\beta_S\left[\frac{\mathrm{kg}}{\mathrm{m^3}}\right]$ and $\beta_C\ \left[\frac{\mathrm{kg}}{\mathrm{m^3}}\right]$ are the expansion coefficients of temperature, salinity concentration and crystal mass fraction, respectively.

It is assumed that the increase in the degree of saturation ($\Delta Se\left[\frac{\mathrm{kg}}{\mathrm{kg}}\right]$) is immediately translated into the crystallization of halite (ΔC) since the brine is saturated. Note that kinetic effects such as nucleation and growth rates are ignored; see Jarvis & Woods (1994). It is further assumed that all of the nucleated crystals settle on the lake floor and accumulate into a uniform layer. This assumption is supported by the footage from the ROV, showing no marks of sliding or erosion; however, to clearly show the importance of erosion of cumulates by currents, additional research is required.

For the case of cooling of a saturated brine solely, the amount of cooling (ΔT) will result in a saturation change (ΔSe) of:

$$\Delta Se = \sigma \Delta T \tag{2}$$

where $\sigma\left[\frac{1}{K}\right]$ is the saturation-temperature relation (Ouillon *et al.*, 2019).

Because saturation with excess translates directly to halite formation, consequently $\Delta C = \Delta Se$. Applying this to Eqs 1 and 2 yields $\Delta\rho = \beta_C \sigma \Delta T$. Note that the effect of cooling on the degree of saturation and halite crystallization is considered, because the influence of temperature on density does not affect the halite formation directly. This can be translated into total crystal mass per unit area ($M_{C,\mathrm{cool}}\ \left[\frac{\mathrm{kg}}{\mathrm{m^2}}\right]$) by multiplying it by the water depth (H [m]), under the assumption that the water column is wellmixed and has a uniform temperature (a reasonable assumption for the Dead Sea during the winter season):

$$M_{C,\mathrm{cool}}\left[\frac{\mathrm{kg}}{\mathrm{m^2}}\right] = \beta_C \sigma \Delta T H \tag{3}$$

The thickness (D_{cool}) of the accumulated halite layer on the lake floor due to cooling per unit area will be:

$$D_{\mathrm{cool}}[\mathrm{m}] = \frac{\beta_C \sigma \Delta T H}{(1-\mathrm{PO})\rho_{\mathrm{NaCl}}} \tag{4}$$

where ρ_{NaCl} is the halite density and PO $[\frac{\mathrm{m^3}}{\mathrm{m^3}}]$ is the halite accumulation layer porosity.

For the case of evaporation solely, the removal of a water layer with thickness e from a saturated brine with initial uniform salinity concentration $S = S_i$ will result in the crystallization and accumulation per unit area of:

$$M_{C,\mathrm{evap}}\left[\frac{\mathrm{kg}}{\mathrm{m^2}}\right] = eS_i\beta_S, \tag{5}$$

yielding:

$$D_{\mathrm{evap}} = \frac{eS_i\beta_S}{(1-\mathrm{PO})\rho_{\mathrm{NaCl}}} \tag{6}$$

Inserting the parameters relevant to the Dead Sea during winter, namely $\sigma = 0.25 \cdot 10^{-3}\left[\frac{1}{\mathrm{K}}\right]$, $\beta_C = 940\ \left[\frac{\mathrm{kg}}{\mathrm{m^3}}\right]$, $\beta_S = 940\left[\frac{\mathrm{kg}}{\mathrm{m^3}}\right], \rho_{\mathrm{Nacl}} = 2160\left[\frac{\mathrm{kg}}{\mathrm{m^3}}\right]$ and $S_i = 0.28\left[\frac{\mathrm{kg}}{\mathrm{kg}}\right]$, as in Ouillon *et al.* (2019), $PO = 0.25\ [\frac{m^3}{m^3}]$(a typical value for rhombohedral packing) yields:

$$D_{\mathrm{cool}} = 0.15 \cdot 10^{-3}\Delta \mathrm{T}\ H \tag{7}$$

$$D_{\mathrm{evap}} = 610 \cdot 10^{-3} \cdot \mathrm{e}. \tag{8}$$

RESULTS

Hourly changes in the thickness and grain size of the accumulated halite

The hourly changes in the thickness of the accumulated halite, captured by the underwater time-lapse camera, are presented in Fig. 6 for both sites of the mixed supersaturated brine and the diluted plume. It was found that halite precipitation is over seven times higher in the mixed supersaturated brine (11.7 mm in 11.5 days, *ca* 1 mm day^{-1}) than in the diluted plume (1.5 mm in 11 days, *ca* 0.14 mm day^{-1}). These observations were conducted with the same underwater time-lapse camera device, with a one-week separation (Fig. 4); the following section presents the environmental conditions driving the precipitation during these two observation periods. From the individual measurements (Fig. 6A), a time series of the accumulated halite thickness (Fig. 6B) and the rate of accumulation (Fig. 6C) was constructed. Under the mixed supersaturated brine, halite accumulates continuously (Fig. 6B) at a high rate (mean accumulation rate of 0.04 mm h^{-1}) and it varies diurnally from low rates (0.01 mm h^{-1}) to a rate eight times higher (0.08 mm h^{-1}). Beneath the

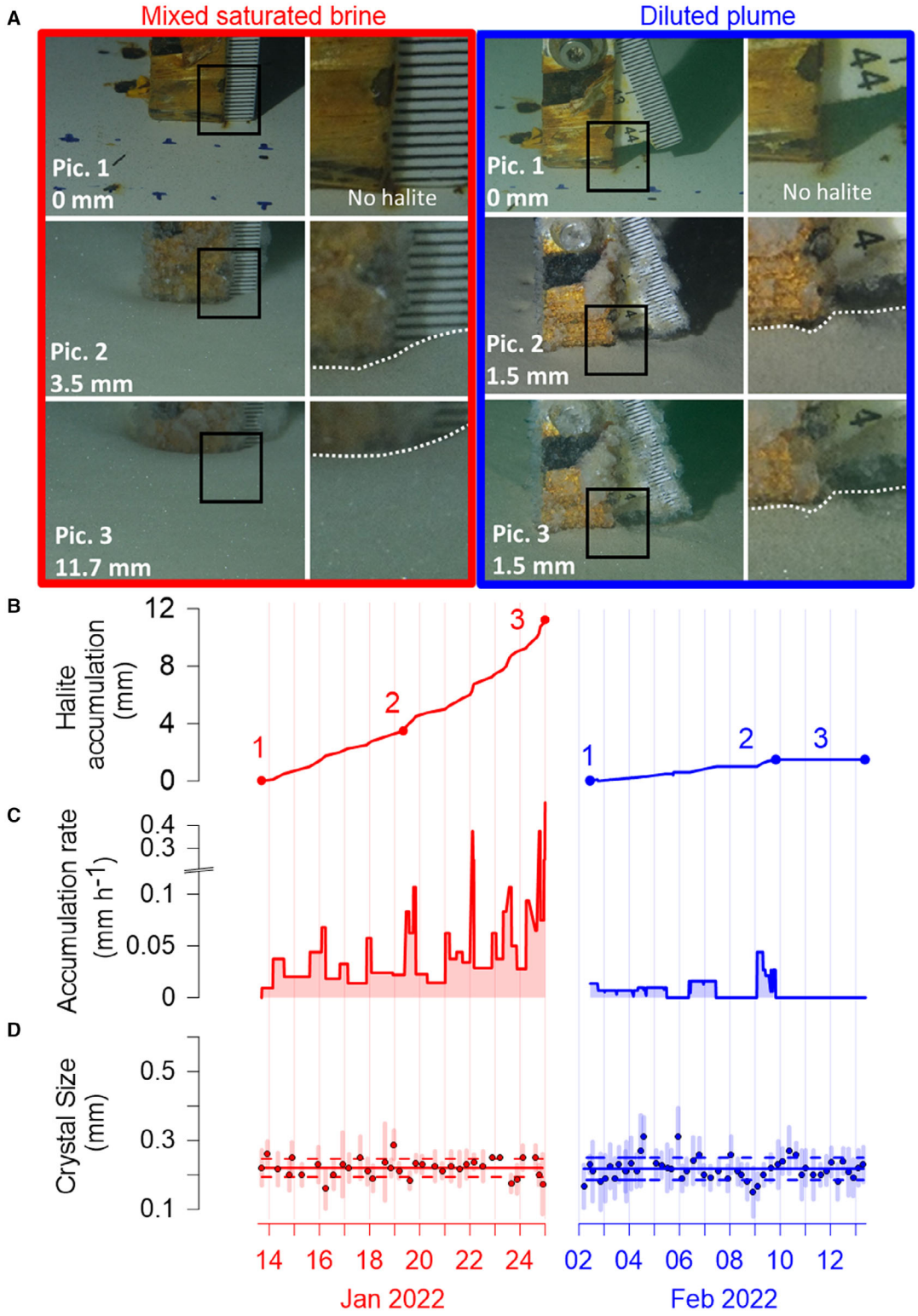

Fig. 6. Halite accumulation at the Dead Sea floor captured by an underwater time-lapse camera (TLC), depicting observations from the mixed supersaturated brine (left side, red) and under the diluted plume (right side, blue). (A) Representative pictures and close-ups; picture timings are indicated in (B) as dots. The time series of (B) accumulated halite thickness and (C) accumulation rate are shown. (D) The time series of halite crystal sizes displays the measured data points with standard deviations for *ca* five measured crystals (depicted as vertical lines), along with the overall mean value of crystal size (solid lines) and its standard deviation (dashed lines).

diluted plume, halite accumulated at significantly lower rates (mean accumulation rate of 0.006 mm h^{-1}) with periods of no halite accumulation (Fig. 6B and C).

The cumulate's crystal size is quite uniform during the observation periods in both environments, showing a unimodal size distribution, with a mean crystal size of 0.22 ± 0.04 mm (Fig. 6D), ranging between 0.1 to 0.6 mm, and 0.05 to 0.55 mm, in the mixed saturated brine and the diluted plume, respectively. The observed winter cumulates have crystal sizes typical for winter halite precipitation that was documented on the Dead Sea lake floor (Sirota *et al.*, 2017) and in the modern (*ca* 40 years) sedimentary record (Sirota *et al.*, 2021). Interestingly, the crystal size did not change, whereas the halite deposition rate varied significantly (Fig. 6C). Furthermore, despite the lower level of supersaturation under the diluted plume (Sirota *et al.*, 2020), the crystal sizes are similar to those measured in the mixed saturated brine environment (Fig. 6D). This finding is intriguing, given the results from Sirota *et al.* (2017) demonstrating that reduced supersaturation typically leads to larger crystal size. A possible explanation for this discrepancy is that the plume was laden with detrital sediment, thereby increasing the number of nucleation sites available for crystal formation. This, in turn, may have counteracted the effect of lower supersaturation, leading to the formation of fine crystals.

Hourly changes in the environmental drivers of halite accumulation

The time series of the environmental drivers, together with the halite accumulation rate on the lake floor in the two different environments, are presented in Fig. 7A to D. The evaporation varies in the diurnal course and the daily average, along the observational periods (Fig. 7B). In the mixed supersaturated brine measurement period, the average evaporation rate is 0.23 mm h^{-1}, in which the daily average greatly varies (for example, day mean value of 0.31 mm h^{-1} on 19 January 2022 versus 0.17 mm h^{-1} on 20 January 2022). Over the course of a day, the evaporation rate can vary from a low rate of 0.1 mm h^{-1} to high peaks of >0.4 mm h^{-1}. In the diluted plume, the evaporation is relatively low during most of the measuring period (*ca* 0.1 mm h^{-1}, average of 0.12 mm h^{-1}), with two days (4 and 10 February 2022) of intense evaporation (mean daily value of *ca* 0.25 mm h^{-1}). The evaporation in the second period of the diluted plume (2 to 13 February 2022) is much lower than that in the first period in the mixed saturated brine (13 to 25 January 2022) due to different weather conditions. Since both stations exhibit a similar pattern of evaporation when measured simultaneously (Fig. S2), there can be a comparison of the halite accumulation in the two environments related to the evaporation rates (see *Variations in halite accumulation rates under a diluted plume – the role of wind/wave mixing and plume stability* and *The influence of diluted plume stability on halite deposition* sections).

The trends in water temperature are presented in Fig. 7C for both environments. The water column cools in both environments, with average rates of 0.036°C day^{-1} and 0.029°C day^{-1} in the mixed supersaturated brine and diluted plume areas, respectively. The hourly rate of temperature change (i.e. heating and cooling) in the mixed supersaturated brine (Fig. 7D) has an absolute value of *ca* 0.15 °C day^{-1}, with two short events of more significant cooling at a rate of *ca* 0.36°C day^{-1}.

Weekly measurements of halite accumulation on the lake floor

The accumulation of halite over observation periods of a few weeks (see timeline in Fig. 4) was characterized through the deployment of concrete blocks on the lake floor at a water depth of *ca* 20 m, at the two observation sites (mixed supersaturated brine – Ein Gedi, and diluted plume – Ein Feshkha springs system). Once deployed, halite accumulates over the flat top of the block. For the documentation of these deposits, the video camera of the ROV was used (see details in *Remotely operated vehicle observations of halite accumulation over a concrete block – weekly resolution* section) (Fig. 3C). The mixed supersaturated brine observations are shown in Fig. 8A to C, and the diluted plume observations in Fig. 8D to F. The halite cover is nearly planar, parallel to the top of the block, and composed of fine crystal cumulate halite (Fig. 8A and D), which seems similar to the textures documented by the underwater time-lapse camera (see *Hourly changes in the thickness and grain size of the accumulated halite* section).

At both concrete blocks, upon the nearly planar halite accumulation, discrete bulges were disregarded during accumulation thickness measurements. It is posited that these formations arise from the detachment and sedimentation of halite fragments (*ca* a few centimetres), which precipitated around the ropes linking the concrete block

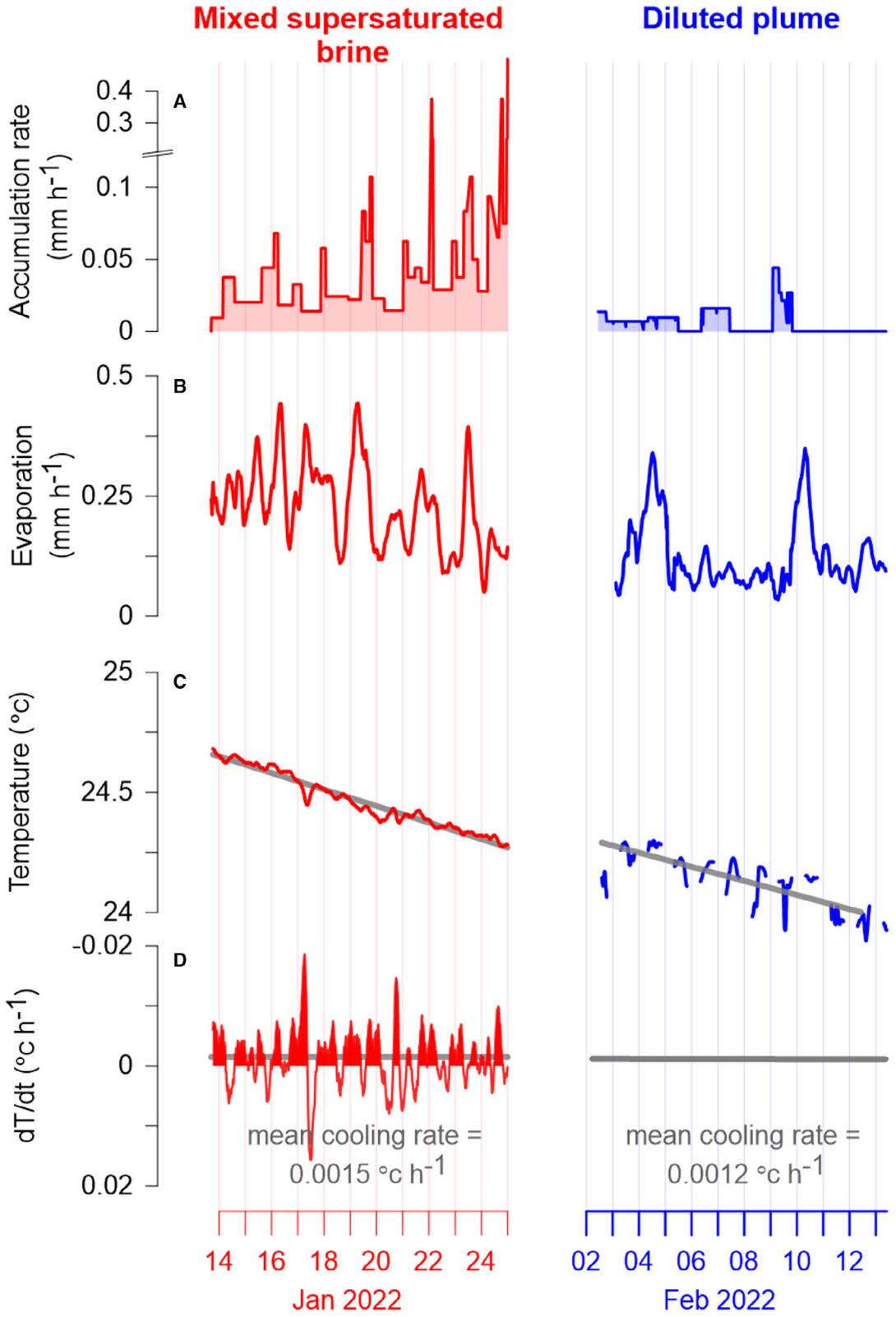

Fig. 7. Time series of halite accumulation rate from the time-lapse camera (TLC) (A) and the environmental drivers, i.e. evaporation rate (B), water temperature (C) and rate of temperature change (D), with the mean cooling rate trend line (grey line). Left panels (EG100-red) – mixed supersaturated brine and right panels – diluted plume (EF-blue). Note that due to a malfunction in the EF buoy electrical system, the temperature data is not continuous.

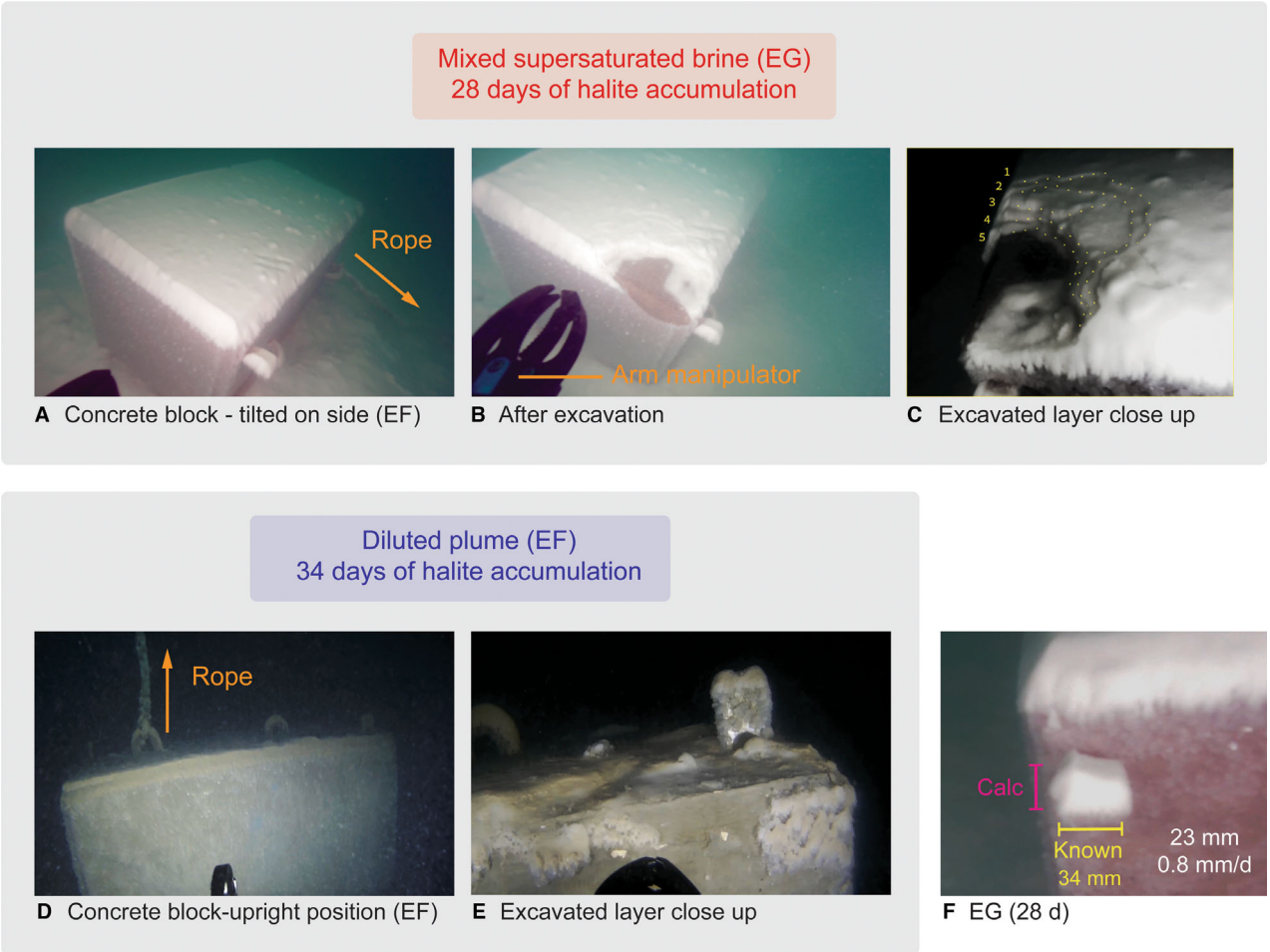

Fig. 8. Halite deposition over concrete blocks. After 28 days of halite accumulation in the mixed supersaturated brine location (A) to (C). (A) The newly formed halite layer before exposing the deposited strata with a remotely operated vehicle (ROV) arm manipulator. (B) After exposure. (C) The exposed accumulated layer shows about five sublayers. After 34 days of halite accumulation in the diluted plume location (D) and (E). (D) The newly formed halite layer. (E) Close-up after exposure. (F) Halite accumulation thickness on the concrete block. The known dimensions of the L-shaped iron scale are marked in yellow lines, and the approximated thickness of the halite is shown in pink lines. See Fig. S3 for the entire set of measurements. Note that the concrete blocks are oriented differently on the lake floor, with the mixed supersaturated brine concrete block lying on its side, resulting in the measurement of the halite accumulated on top of the L-shaped iron scale. Another indicator of the higher precipitation rate in the mixed supersaturated brine area compared to the diluted plume is observed with the rope and floating barrel: they float upright in the diluted plume (D), whereas in the mixed supersaturated brine, they are covered by enough halite to lie draped across the lake floor (A).

and the floating barrels above (utilized as sonar reflectors). It is noteworthy that, within the underwater time-lapse camera, no analogous phenomena were observed, as there were no floating objects present. Additionally, the halite covering on the barrels exhibits a smooth and planar configuration. After documenting the newly formed halite layer, nearly vertical outcrops at the corner of the blocks were exposed using the ROV manipulator arm (Fig. 8B and E) to observe vertical variations of the halite strata (Fig. 8C). The thickness of the cumulated layer was measured by its comparison with the known size of the L-shaped iron angle (Fig. 8F; Fig. S3). Halite thickness in both environments was examined twice (see timeline in Fig. 4).

In the mixed supersaturated brine, halite thickness measured 11.4 mm and 23 mm on the 15th and 28th days from installation of the concrete blocks, respectively. A mean rate of

0.82 mm day^{-1} for the entire measurement period was calculated, with rates of 0.76 mm day^{-1} for the first 15 days and 0.90 mm day^{-1} for the last 13 days, respectively (Fig. S3B and C). The accumulated fine halite layer comprises approximately five sublayers (Fig. 8C), all made of fine halite cumulates. Since intact samples could not be collected, there is no direct evidence of the grain contacts and degree of cementation. However, these cumulates can be compared to those studied petrographically in coastal exposures (Sirota *et al.*, 2021). There, one can observe similar winter cumulate halite layers, composed of the same sub-layers, with slight cementation between the cumulate crystals. For further discussion, see *Sub-layering of halite cumulates controlled by evaporation* and *Application to halite records* sections.

In the diluted plume, the halite thickness measured *ca* 2.0 mm and 16 mm on the 15th and 34th days from installation of the concrete blocks, respectively. A mean rate of 0.47 mm day^{-1} for the entire measurement period was calculated, with rates of 0.14 mm day^{-1} for the first 15 days and 0.74 mm day^{-1} for the last 19 days, respectively (Fig. S3D to F). The significant variation in accumulation rate under the diluted plume is discussed in *The influence of diluted plume stability on halite deposition* section.

Variations in halite accumulation rates under a diluted plume – the role of wind/wave mixing and plume stability

Halite accumulation variations under the diluted plume and the environmental drivers are presented in Fig. 9A to E, based on three different periods of measurement (see *Hourly changes in the thickness and grain size of the accumulated halite* and *Hourly changes in the environmental drivers of halite accumulation* sections for the underwater time-lapse camera and ROV observation details). Over these periods, the halite accumulation rate is examined as the integral over the entire period. Along several days, halite accumulation under the diluted plume varies from a relatively low accumulation rate of 0.14 mm day^{-1} (Fig. 9A, period 1 – purple, and period 3 – blue) to a relatively high accumulation rate of 0.75 mm day^{-1} (Fig. 9A, period 2 – orange), a range by a factor of 5. In contrast, in the mixed supersaturated brine environment, the halite accumulation rate remains constantly high at 0.76 mm day^{-1} and 0.9–1.0 mm day^{-1} (Fig. 9A, grey, in periods 1 and 2, respectively).

The evaporation rate varies as well, though in a less significant manner; evaporation time series are presented in Fig. 9C, showing the mean value of the evaporation rate for each period. Over a week, the average evaporation rate varies by a factor of *ca* 1.5 (periods 1 and 3 with 2.7 to 3.0 mm day^{-1} and period 2 with 3.9 mm day^{-1}). To examine the relationship between the evaporation rate and halite accumulation, the ratio of total evaporation thickness (Fig. 9C) to halite accumulation thickness (Fig. 9A) was analysed, which led to determining the amount of evaporation required for the accumulation of a certain thickness of halite on the lake floor. This evaporation to halite ratio, presented in Fig. 9B, varies by a factor of 4 over weekly periods under the diluted plume (periods 1 and 3 with 19–20 and period 2 with 5). Next, the environmental factors responsible for this significant shift in the ratio between evaporation rate and halite accumulation were identified.

The daily patterns in wind speed and wave amplitude are presented in Fig. 9D and E, respectively. A high wind speed generates high amplitude waves as occurred in period 2 with seven windstorms (7 to 11 m s^{-1}); during these storms, the diluted plume stability threshold is exceeded with wind speed >4 m s^{-1} (Mor *et al.*, 2018, 2021). Such conditions increase vertical mixing in the diluted plume and coincide with a surge in halite accumulation, along with rises in evaporation rate. Practically, the plume diminished and the evaporation to halite ratio decreased significantly to *ca* 5 : 1, aligning more closely with the relatively constant ratio observed in the mixed supersaturated brine environment (Fig. 9B). In contrast, during periods of relatively weak wind–wave intensities (wind speed <4 m s^{-1}, periods 1 and 3, Fig. 9D and E) the plume is more stable. Then, high ratios of *ca* 20:1 were documented indicating that four times higher evaporation thickness is needed for a given halite accumulation thickness.

DISCUSSION

Hourly halite accumulation rate as controlled by evaporation

Explored here is the mechanistic relationship between the observed halite accumulation and the measured environmental drivers, i.e. evaporation and water cooling. To assess the contribution of these two primary drivers, halite accumulation

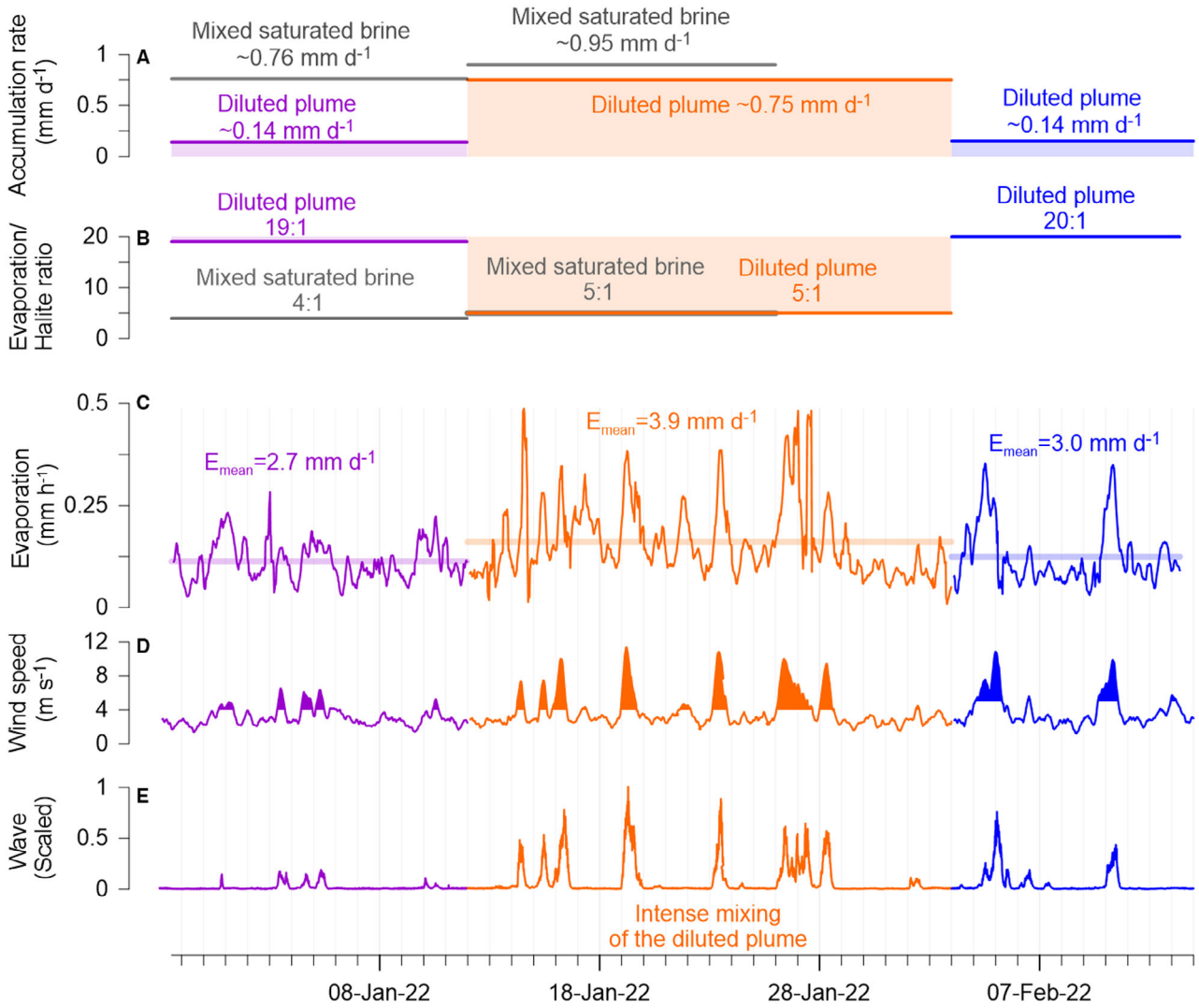

Fig. 9. Halite accumulation varied under the diluted plume, with environmental drivers examined over three periods (represented by different colours: purple for period 1, orange for period 2 and blue for period 3, as shown in the timeline in Fig. 4). (A) Mean halite cover rate: The data for the diluted plume in periods 1 and 2 are based on remotely operated vehicle (ROV) observations (totals of 2.0 mm and 14.0 mm, respectively), while data for period 3 is based on the time-lapse camera (TLC) observation (total of 1.5 mm). For the mixed supersaturated brine accumulation rate, shown in grey, period 1 is based on ROV observation (a total of 11.26 mm), while period 2 presents the mean value derived from integrated TLC observations and ROV, at 1.0 mm day^{-1} (a total of 11.7 mm) and 0.9 mm day^{-1} (a total of 11.74 mm), respectively. (B) The ratio of evaporation rate to halite deposition rate. (C) Evaporation rate (mean value for each period is presented). (D) Wind speed (with 4 m s^{-1} diluted plume stability threshold based on Mor *et al.*, 2018, 2021), and (E) scaled wave amplitude. Note that higher winds and waves decrease the stability of the plume (see text).

over time was calculated using the mass conservation model presented in the *Theoretical relation between evaporation, water cooling and halite accumulation* section applied to the measured environmental forcing. This high-resolution examination is achievable solely in the mixed supersaturated brine (and not in the diluted plume) due to the comparatively straightforward relationships among evaporation, cooling and halite accumulation. Figure 10 presents the observed and calculated halite accumulation thickness and rate from the mixed saturated brine. The total calculated halite accumulation ($D_{tot} = D_{cool} + D_{evap}$) agrees with the observed accumulation and reinforces the model; the calculated halite cover is 97% of the measured halite cover

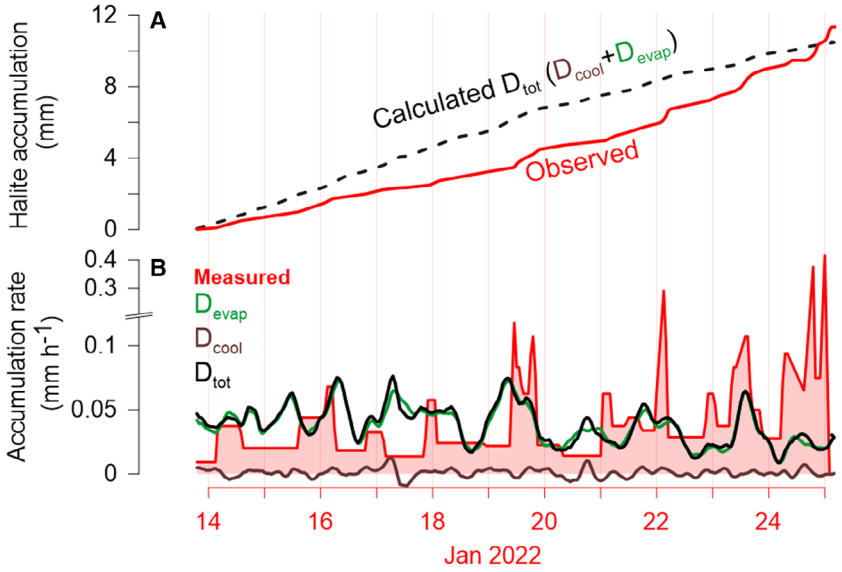

Fig. 10. Quantifying halite accumulation by combining direct observations with a theoretical model. (A) Time series of measured (red solid line) and calculated (black dashed line) halite accumulation. (B) The measured halite accumulation rate shows a sub-diurnal cycle. The calculated accumulation rate (D_{tot}) is based on the relative contribution of evaporation (D_{evap}, green) and water cooling (D_{cool}, brown). The evaporation contribution shows values similar to the measured values, including the sub-diurnal pattern. The contribution of water cooling to the calculated halite accumulation is minor. Note that the measured halite accumulation is from the time-lapse camera (TLC) located at Ein Gedi (EG), and the evaporation and cooling rates were measured from the nearby platform, EG100 (Fig. 2).

(11.4 mm and 11.75 mm, respectively) (Fig. 10A). The contribution of evaporation (D_{evap}) to halite accumulation is on the order of magnitude of the measured accumulated halite rate, and it is *ca* ten times larger than the calculated halite accumulation following the cooling of the water column (D_{cool}) (Fig. 10B). Thus, the halite accumulation rate on the lake floor is dictated by the evaporation rate and its variations. When assessing a deep water body with a slow response time to changes in lake heat storage, daily-scale cooling events do not significantly alter the water column temperature (Hamdani *et al.*, 2018; Tau *et al.*, 2022). Consequently, the degree of halite saturation remains stable. This implies that the impact of brine cooling on the degree of halite saturation and halite deposition rate on an hourly–weekly scale is minor compared to the major role of brine cooling on the seasonal scale (Sirota *et al.*, 2016).

The influence of diluted plume stability on halite deposition

The stability of the diluted plume plays a crucial role in halite precipitation. A wide range in the ratio between evaporation and halite accumulation was observed. This ratio is up to four times larger when the plume is stable and is linked to wind and wave intensity (5 : 1 versus 20 : 1, Figs 9, 11A and 11B). Furthermore, to estimate the predicted accumulation of halite due to evaporation from the diluted area without the dilution effect, the model that accounts for saturated and mixed water columns was used (Fig. 11B and C). At relatively low wind and wave intensities in the diluted area, the calculated halite cover (without the dilution effect) is much higher than the observed halite cover by a factor of *ca* 3.3 (with factors of 3.1 for period 1 and 3.5 for period 3); this deviation is attributed to the dilution effect (Fig. 11B right panel, Fig. 11C, diluted plume periods 1 and 3). When wind and waves intensify in the diluted area, the calculated halite and measured halite show similar values, akin to those observed in the mixed supersaturated area (Fig. 11C). During the diluted plume period 2, the measured halite is 93% of the calculated halite, while during the mixed supersaturated brine period 2, the measured halite corresponds to 103% and 100% of the calculated halite for underwater time-lapse camera and concrete data, respectively.

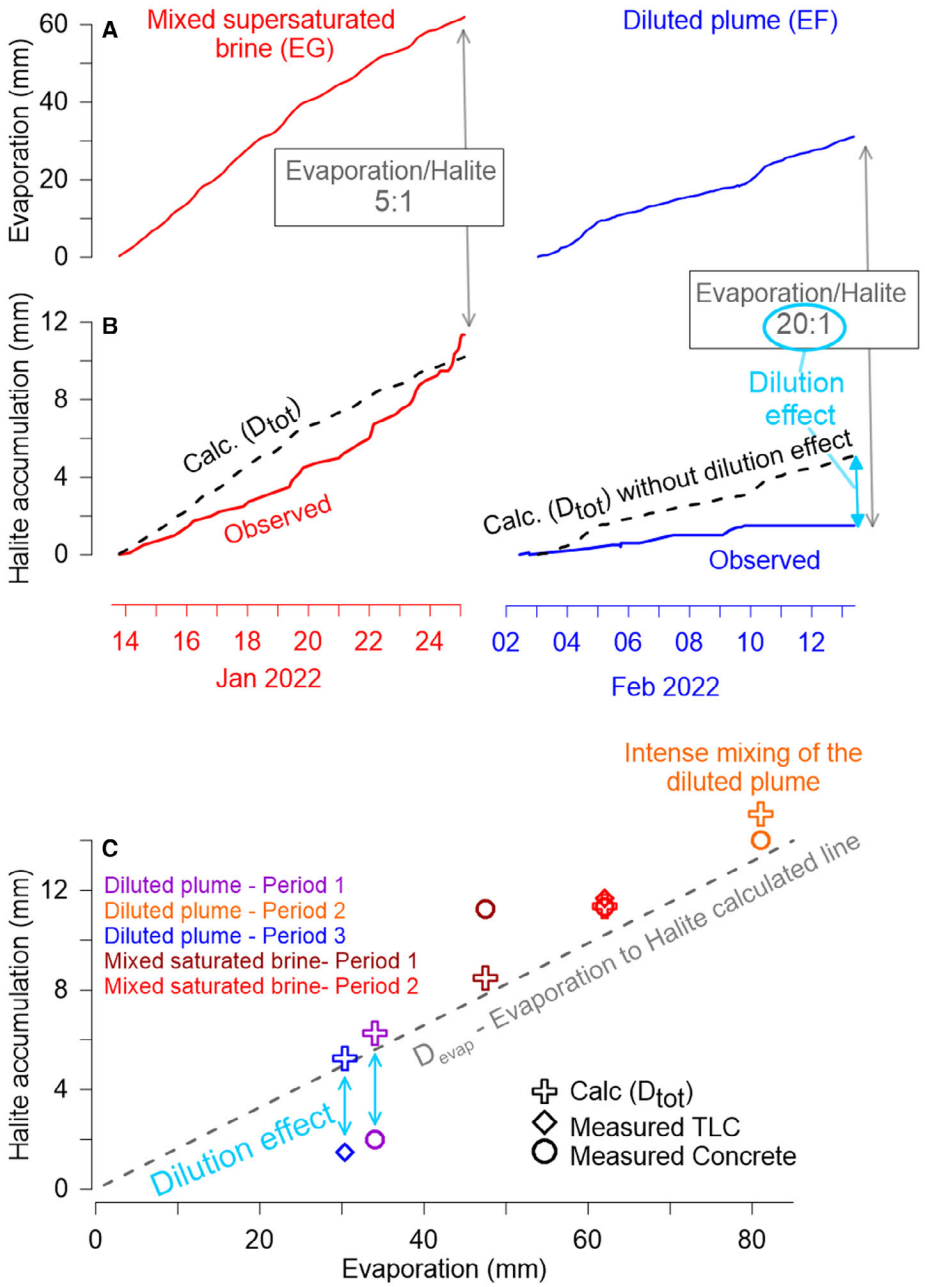

Fig. 11. Comparison of halite accumulation and evaporation in the mixed supersaturated brine and the diluted plume environments (red and blue, accordingly). Time series of (A) evaporation (accumulated) and (B) halite accumulation based on time-lapse camera (TLC) campaigns; note the different timelines on the X-axis, according to the above-mentioned colour coding. Measured and calculated halite cover are presented; the calculated halite accumulation is based on the theoretical model. Note that the calculated halite model does not take into account the dilution effect in the diluted plume environment. The dilution effect on halite accumulation is demonstrated by: (i) the ratio between evaporation and halite accumulation – 5 : 1 and 20 : 1, in the mixed supersaturated brine and diluted plume area, respectively; and (ii) the lack of the measured accumulated halite, compared to the calculated halite without the dilution effect (30%, 1.5 mm versus 5.1 mm). (C) Calculated and measured halite thickness. The calculated halite thickness (cross) and the measured halite thickness from the TLC (square) and the concrete (circle) campaigns. A line describing the theoretical relationship between evaporation and halite thickness is denoted by the dashed grey line. Note that in the mixed saturated brine during period 1, the measured halite is 132% of the calculated halite. It's essential to emphasize that this disparity, attributable to potential errors in both measurement and calculation, suggests that more halite accumulates than anticipated by the model. This stands in contrast to the diluted plume environment, where significantly less halite is accumulated than calculated.

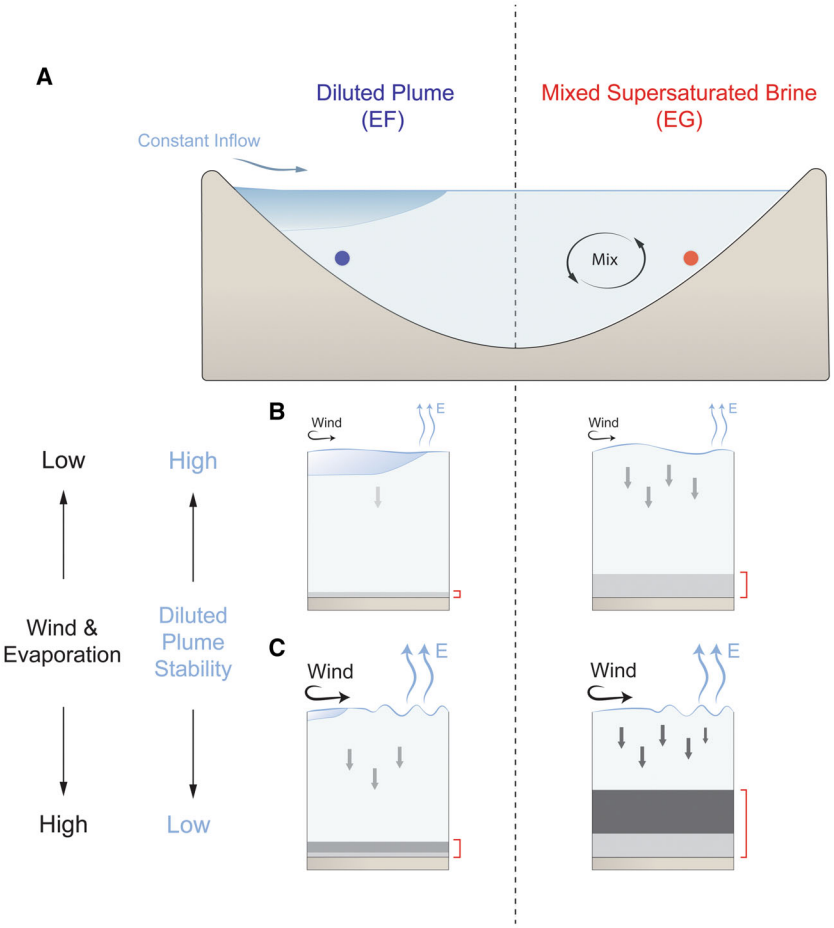

Fig. 12. Graphical summary. (A) The two different environments in the hypersaline water body; on the left, the diluted plume area, and on the right the mixed supersaturated brine area, far from freshwater inflows. (B) and (C) The effect of increasing wind speed and evaporation (*Y*-axis) on accumulated halite in each environment is shown; in the mixed supersaturated brine environment, higher wind speed and evaporation result in a higher accumulation rate. In the diluted plume, increased wind and wave activity mix the diluted plume and significantly increase the halite accumulation rate, which was initially low compared to the mixed supersaturated brine environment.

The different states of evaporation along with plume stability and their influence on halite accumulation are schematically presented in Fig. 12A to C. In the mixed hypersaline brine, low evaporation results in low halite accumulation (Fig. 12B, right), while high evaporation results in intense halite accumulation (Fig. 12C, right). In the diluted plume, under low wind speeds, the buoyant diluted plume is stable due to freshwater dilution, with low-salinity brine overlying the saltier Dead Sea brine, resulting in either no halite accumulation beneath the plume or a very low accumulation rate if supersaturated brine reaches from the mixed supersaturated brine area (Fig. 12B, left). However, as wind speed increases, the upper diluted layer mixes with the underlying saltier Dead Sea brine which crops out to the lake surface, resulting in reduced stability and further mixing of supersaturated brine even up to the total elimination of the plume effect. This cancels the effect of the diluted plume, leading to increased halite accumulation in the area near the freshwater inflows, in a fashion similar to that of the non-diluted area of the water body, far from freshwater inflows (Fig. 12C, left).

Sub-layering of halite cumulates controlled by evaporation

Global halite deposits are characterized by fine lamination (millimetres thick) (Lowenstein, 1988;

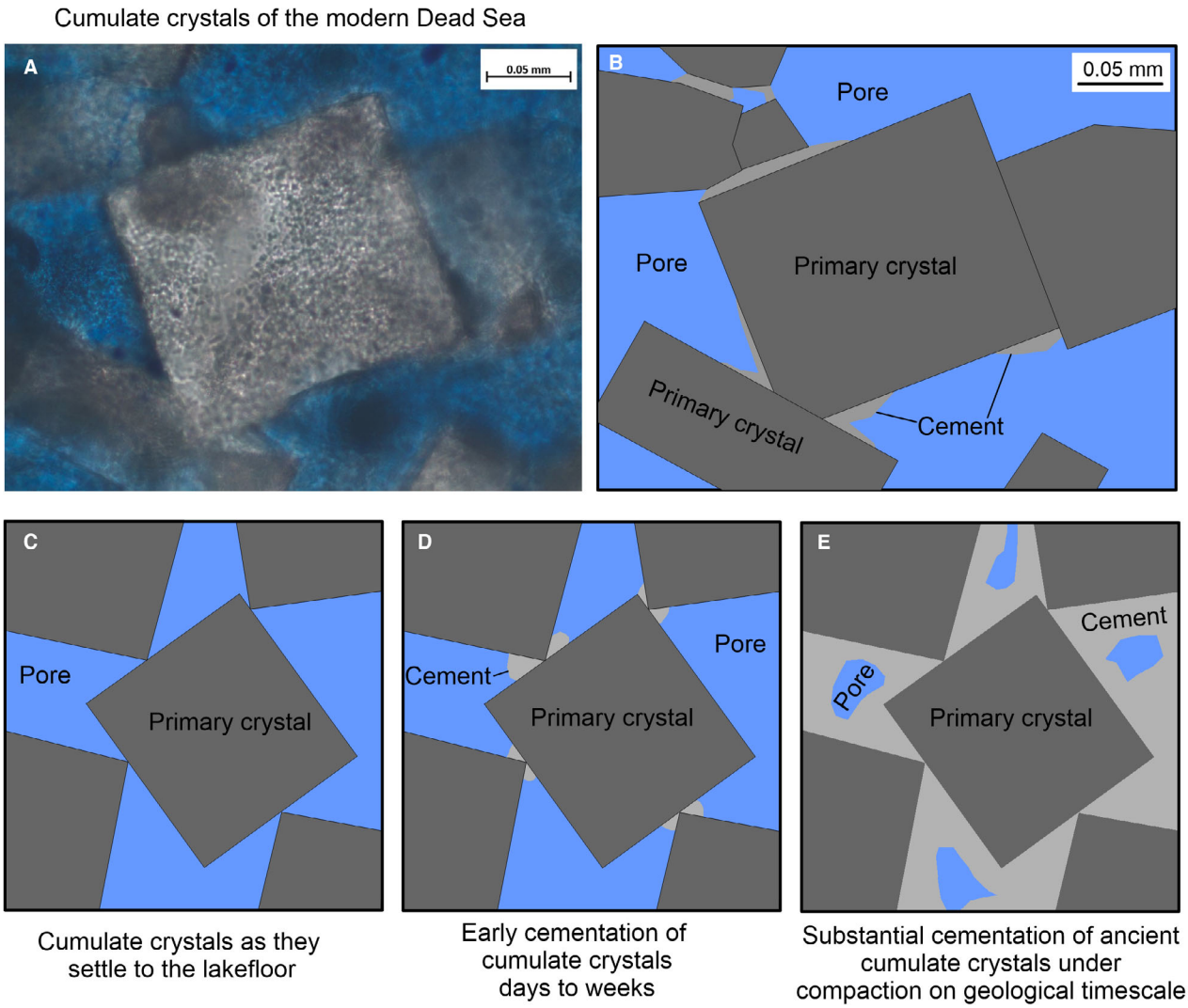

Fig. 13. The cementation process of cumulate crystals. (A) Thin section image (plane polarized light) and (B) schematic illustration showing cumulate crystals from a modern halite sequence from the Dead Sea shore (adapted from Sirota *et al.*, 2021). Schematic illustration of (C) cumulate crystals settling to the lake floor without cementation. (D) Slight cementation between cumulate crystals occurs days to weeks after settling, while still in contact with the supersaturated brine. This initial cementation minimally fills the pores between crystals, resulting in high porosity of modern non-compacted halite cumulates. (E) Halite cumulates with low porosity after diagenesis and compaction, significantly reducing halite porosity.

Li *et al.*, 1996; Kirkland *et al.*, 2000; Benison & Goldstein, 2001; Hovorka *et al.*, 2007; Jagniecki & Lowenstein, 2015) including late Quaternary halite sections in the Dead Sea basin (Kiro *et al.*, 2016; Palchan *et al.*, 2017; Sirota *et al.*, 2021). It is proposed here that the sub-seasonal layering of the cumulate halite layer (Fig. 8C), which forms during winters, reflects variations in evaporation rate. Each sublayer can be interpreted as an evaporation event that drives a pulse of halite cumulates. Slight oversaturation of the brine at the brine–sediment interface imposes a constant cementation rate for settled (cumulate) crystals as they are in contact with the supersaturated brine prior to their burial. Modern halite layers show only slight cementation after burial and before long-term compaction (Fig. 13A and B; Sirota *et al.*, 2021). The diagenesis of halite layers can be divided into three stages: (i) cumulate crystals settle to the lake floor (Fig. 13C); (ii) within hours to days, slight cementation forms, maintaining high porosity

(Fig. 13D); and (iii) subsequent diagenesis and compaction reduce the porosity of the halite cumulate layers (Fig. 13E) (Casas & Lowenstein, 1989).

The variation in evaporation rates and the following variation in accumulation rate are reflected in stage 2 (Fig. 13C). Slow accumulation results in extended cementation periods, characterized by a harder surface, whereas fast accumulation leads to a softer layer, exemplified by the sub-layering of winter cumulate halite (Fig. 8C). Therefore, synoptic-scale atmospheric circulation that generates wind–wave storms over the Dead Sea (Eyal *et al.*, 2023), enhances evaporation (Lensky *et al.*, 2017; Hamdani *et al.*, 2018) and may manifest in the sublayers observed in the halite sequence (refer to *Application to halite records* section for further elaboration).

Application to halite records

The novel contribution of this study lies in identifying the dominant factors affecting halite precipitation across various timescales. It was found that over short timescales, evaporation plays a more significant role in halite precipitation than temperature. Previous studies have indicated that temperature dominates at longer timescales; in the hypersaline and monomictic Dead Sea, seasonal variations are pronounced, leading to distinct alternations in halite sequences between summer and winter layers due to thermohaline stratification and the influence of brine temperature on halite saturation (Sirota *et al.*, 2016, 2017, 2021). The exposed modern halite sequence from *ca* 34 years of halite precipitation in the Dead Sea (Fig. 14A; Sirota *et al.*, 2021) is characterized by seasonal varves of halite deposits (see Sirota *et al.*, 2021, for more details). The summer layers with coarse and consolidated crystals become thinner up-section (Fig. 14A and B), while the winter layers, made of cumulate halite are the main component of the total halite sequences (Fig. 14A and B; Sirota *et al.*, 2021). During winter, halite deposition generates cumulate halite layers that are comprised of several sub-layers (Fig. 14B), with interbedded layers of detrital material following flash floods.

The relative thickness of the cumulate halite from both underwater time-lapse camera and concrete blocks is depicted on a hand specimen from a modern halite sequence on the Dead Sea shore in the Ein Gedi region (Fig. 14B). This illustration implies that this study's measurements do not encompass the entire winter layer. Given longer measurement periods, a slower rate of accumulation is anticipated, possibly accompanied by detrital sediment layers following flash floods. Similar to the slower accumulation rate in the diluted plume area (see *Variations in halite accumulation rates under a diluted plume – the role of wind/wave mixing and plume stability* and *The influence of diluted plume stability on halite deposition* sections), periods characterized by freshwater floods, which lower halite saturation, will likely result in reduced halite accumulation rates, if any (see *Freshwater inflows* section). Furthermore, a discrepancy in the halite accumulation rate was found, which supports the hypothesis that the majority of winter halite deposition occurs during discrete evaporation events. Direct measurements using an underwater time-lapse camera and concrete blocks captured a rapid accumulation rate ranging between 0.7 mm day^{-1} and 1 mm day^{-1} in the Ein Gedi region, surpassing previous measurements for the area. For comparison, an average winter halite deposition rate of 0.25 to 0.5 mm day^{-1} has been derived from the thickness of cumulate halite layers in outcrops along the Dead Sea coast (Sirota *et al.*, 2021). Additionally, a halite crystallization rate of approximately 0.5 mm day^{-1} has been noted along a vertical cable (Sirota *et al.*, 2016). Although this method was employed as a proxy for variations in halite saturation rather than a direct measurement of accumulation on the lake floor, it gives a reference for potential halite production over time.

The identification of sub-seasonal layering within the winter cumulate layer, reflecting evaporation events that drive pulses of halite deposition (see *Hourly halite accumulation rate as controlled by evaporation* section), offers valuable insights into the nature of sub-seasonal layering in halite deposits. Insights can be drawn from two main petrographic features observed in this study:

1 Only slight cementation of cumulate halite crystals occurs at the brine–sediment interface before they are buried and disconnected from the supersaturated brine (Figs 13 and 14). Thus, layers of highly cemented halite cumulate (Fig. 13E) suggest substantial sediment burial, exceeding tens of metres (Casas & Lowenstein, 1989).

2 The laminated structure of the accumulated halite (Fig. 14C), controlled by evaporation, resembles the lamination seen in winter halite cumulate layers in the decadal-scale halite section on the Dead Sea shore (Fig. 14A and B), as

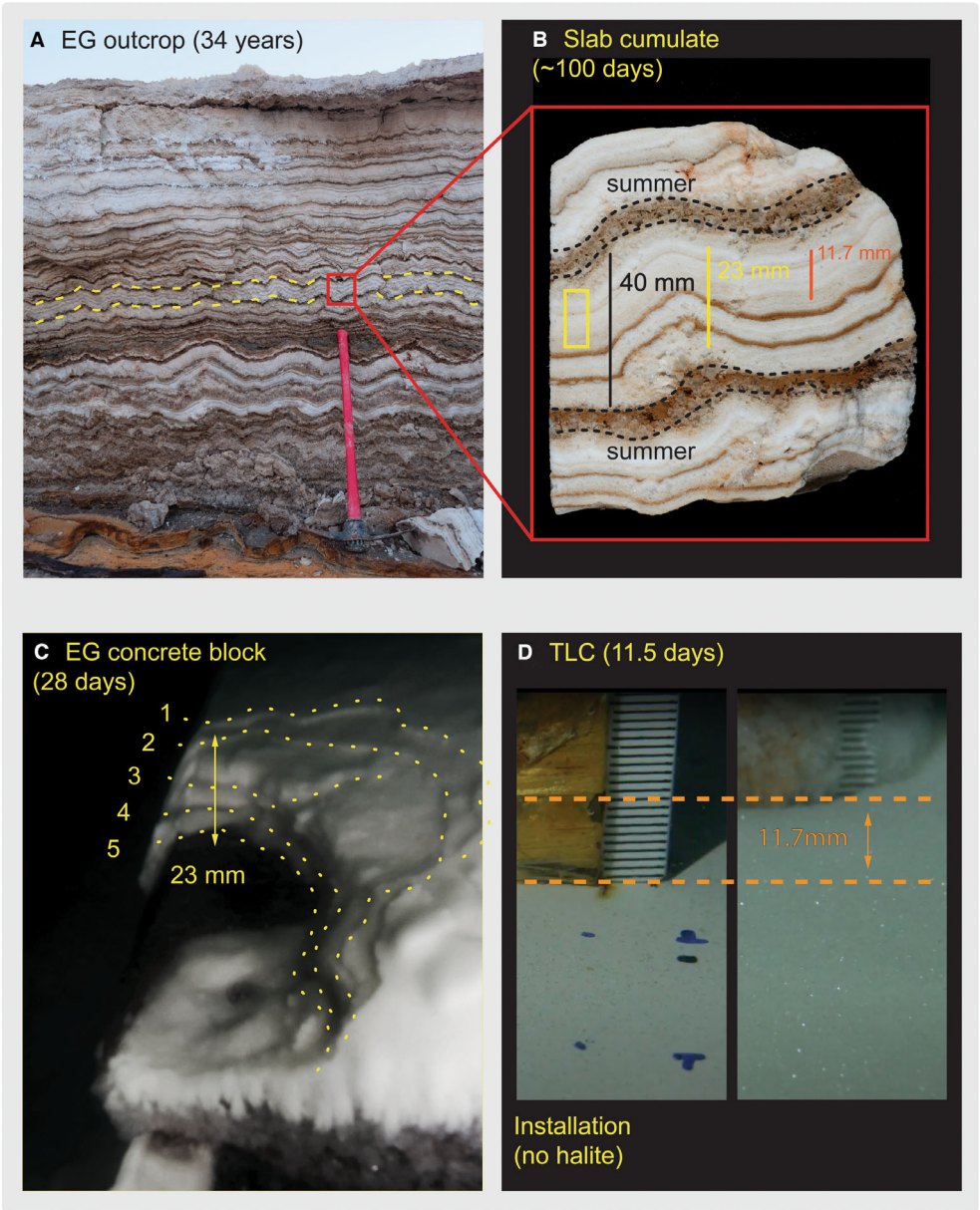

Fig. 14. A zoom-in from an exposed modern halite sequence to the resolution of halite deposition on an hourly timescale. (A) Modern halite sequence on the Dead Sea shore in the Ein Gedi (EG) region (Sirota *et al.*, 2021); (B) a hand specimen sampled from the outcrop in (A). (C) The concrete block in mixed supersaturated brine was observed 28 days after installation, with the section exposed by the remotely operated vehicle (ROV) arm revealing at least five layers within the total 23 mm halite sequence. (D) The underwater time-lapse camera (TLC) from mixed supersaturated brine, showed 11.7 mm of cumulated halite in 11.5 days. Note that the thickness of the cumulate halite from both the concrete blocks (C) and TLC (D) is depicted on a hand specimen (B), indicating that the study's observations do not capture the entire winter accumulation. The area in the hand specimen with similar layering, as captured on the concrete block, is marked with a yellow rectangle.

well as the sub-seasonal layering observed in the Early Holocene and Last Interglacial halite from the Dead Sea basin (Kiro *et al.*, 2016; Brall *et al.*, 2022) and elsewhere (Manzi *et al.*, 2012; García-Veigas *et al.*, 2013; Jagniecki & Lowenstein, 2015). This similarity underscores the utility of such archives for reconstructing discrete environmental events.

SUMMARY AND CONCLUSIONS

1 The study employed novel methodologies to measure *in situ* halite accumulation on the hypersaline lake floor: (i) an underwater time-lapse camera, enabling high-resolution recording of halite accumulation at 0.25 mm intervals (hourly scale) and halite crystal size; and (ii) sedimentation of halite over concrete blocks deployed and observed by an underwater remotely operated vehicle (ROV), allowing observation of halite accumulation over weekly periods.

2 Using these methodologies, two fundamental environments were investigated: a mixed supersaturated brine and a diluted plume resulting from spring discharge. The focus was on deposition during winter, when the halite accumulation rate is highest, the water column is mixed, and the relationship between evaporation and halite accumulation is most straightforward.

3 In the mixed supersaturated brine, halite accumulates at a high average rate of 0.7 to 1.0 mm day^{-1}, with an evaporation to halite ratio of 5 : 1. In contrast, in the diluted plume, under calm winds when the plume is relatively stable, the halite accumulation rate is much lower (0.14 mm day^{-1}), and the evaporation to halite ratio is 20 : 1. To accumulate a certain thickness of halite on the lake floor, four times more evaporation is required. However, when the diluted plume undergoes more frequent mixing by wind-driven waves, the halite accumulation rate is high (0.75 mm day^{-1}), with an evaporation to halite ratio similar to that of the mixed supersaturated brine.

4 The simplified theoretical model for predicting the accumulated halite layer given the environmental forcing, together with observations, shows that the evaporation rate dictates the halite accumulation rate in a fully mixed supersaturated hypersaline water body over the subdiurnal timescale, while temperature dominates over seasonal timescales. The calculated halite thickness resulting from evaporation is *ca* ten times higher than the calculated halite thickness following the cooling of the water column.

5 Sub-seasonal layering comprising the winter cumulate halite layer is formed by the combination of fluctuating halite accumulation driven by changes in evaporation rate and constant cementation of halite crystals at the sediment–water interface. Slower halite accumulation, between evaporation events, extends the cementation periods, resulting in a harder surface, whereas fast accumulation during evaporation episodes leads to a softer layer, exemplified by the sub-layering of winter cumulate halite.

6 The wind speed intensity and duration, controlled by the synoptic-scale atmospheric circulation of Mediterranean cyclones, dictate sub-seasonal halite accumulation on the lake floor during winter. The identification of sub-seasonal layering within the winter cumulate layer, reflecting evaporation events that drive pulses of halite deposition and modify the settled cumulate cementation, offers valuable insights into the nature of sub-seasonal layering in halite deposits.

ACKNOWLEDGEMENTS

We acknowledge Raanan Bodzin, Uri Malik, Alon Moshe, the *R/V Taglit* team (Silvy Gonen, Meir Yifrach, and Shachar Gan-El), and the *R/V Salty Landscapes* team (Jake Ben Zaken, Orit Ben Zaken and Kochav Levy), for their field assistance; Astral-Subsea Marine Robotics (Oded Ezra) for the underwater time-lapse camera design and production, and the ROV surveys; and Yoav Balaban for graphic illustrations. We thank the editor, Alex Brasier, the associate editor, Ashleigh Hood, and two anonymous reviewers for their constructive comments. Financial support was also provided by ISF grant 1471/18 (to NL).

DATA AVAILABILITY STATEMENT

The data that support the findings of this study are available from the corresponding author upon reasonable request.

REFERENCES

Abelson, M., **Yechieli, Y.**, **Crouvi, O.**, **Baer, G.**, **Wachs, D.**, **Bein, A.**, **Shtivelman, V.**, et al. (2006) Evolution of the Dead Sea sinkholes. In: *New frontiers in Dead Sea paleoenvironmental research*, Special Paper. **401**. (Ed. Enzel, Y.), pp. 253–241. Geological Society of America, Boulder, CO.

Abelson, M., **Yechieli, Y.**, **Baer, G.**, **Lapid, G.**, **Behar, N.**, **Calvo, R.** and **Rosensaft, M.** (2017) Natural versus human control on subsurface salt dissolution and development of thousands of sinkholes along the Dead Sea coast. *Case Rep. Med.*, **122**, 1262–1277.

Alpert, P., **Neeman, B.U.** and **Shay-El, Y.** (1990) Climatological analysis of Mediterranean cyclones using ECMWF data. *Tellus A Dyn. Meteorol. Oceanogr.*, **42**, 65–77.

Anati, D.A. and **Stiller, M.** (1991) The post-1979 thermohaline structure of the Dead Sea and the role of double-diffusive mixing. *Limnol. Oceanogr.*, **36**, 342–353.

Anati, D.A., **Stiller, M.**, **Shasha, S.** and **Gat, J.R.** (1987) Changes in the thermo-haline structure of the Dead Sea: 1979–1984. *Earth Planet. Sci. Lett.*, **84**, 109–121.

Anderson, R.Y. (1982) A long geoclimatic record from the Permian. *J. Geophys. Res. Ocean.*, **87**, 7285–7294.

Arnon, A., **Selker, J.S.** and **Lensky, N.G.** (2016) Thermohaline stratification and double diffusion diapycnal fluxes in the hypersaline Dead Sea. *Limnol. Oceanogr.*, **61**, 1214–1231.

Arthurton, R.S. (1973) Experimentally produced halite compared with Triassic layered halite-rock from Cheshire, England. *Sedimentology*, **20**, 145–160.

Benison, K.C. and **Goldstein, R.H.** (1999) Permian paleoclimate data from fluid inclusions in halite. *Chem. Geol.*, **154**, 113–132.

Benison, K.C. and **Goldstein, R.H.** (2000) Sedimentology of ancient saline pans: an example from the Permian Opeche Shale, Williston Basin, North Dakota, USA. *J. Sediment. Res.*, **70**, 159–169.

Benison, K.C. and **Goldstein, R.H.** (2001) Evaporites and siliciclastics of the Permian Nippewalla Group of Kansas, USA: a case for non-marine deposition in saline lakes and saline pans. *Sedimentology*, **48**, 165–188.

Benison, K.C., **Bowen, B.B.**, **Oboh-Ikuenobe, F.E.**, **Jagniecki, E.A.**, **LaClair, D.A.**, **Story, S.L.**, **Mormile, M.R.** and **Hong, B.-Y.** (2007) Sedimentology of acid saline lakes in southern Western Australia: newly described processes and products of an extreme environment. *J. Sediment. Res.*, **77**, 366–388.

Bernau, J.A. and **Bowen, B.B.** (2021) Depositional and early diagenetic characteristics of modern saline pan deposits at the Bonneville Salt Flats, Utah, USA. *Sedimentology*, **68**, 2450–2472.

Bernau, J.A., **Bowen, B.**, **Pardyjak, E.R.** and **Kipnis, E.L.** (2022) Diurnal to Seasonal Dynamics of Groundwater, Evaporation, and Hydrology Fluctuations at the Bonneville Salt Flats Saline Pan. ESS Open Archive.

Beyth, M., **Gavrieli, I.**, **Anati, D.** and **Katz, O.** (1993) Effects of the December 1991—May 1992 floods on the Dead Sea vertucal structure. *Isr. J. Earth Sci.*, **41**, 45–48.

Bowen, B.B., **Kipnis, E.L.** and **Raming, L.W.** (2017) Temporal dynamics of flooding, evaporation, and desiccation cycles and observations of salt crust area change at the Bonneville Salt Flats, Utah. *Geomorphology*, **299**, 1–11.

Brall, N.S., **Gardien, V.**, **Ariztegui, D.**, **Sorrel, P.**, **Guillerm, E.** and **Caupin, F.** (2022) Reconstructing lake bottom water temperatures and their seasonal variability in the Dead Sea Basin during MIS5e. *Depos. Rec.*, **8**, 616–627.

Butler, G.P. (1969) Modern evaporite deposition and geochemistry of coexisting brines, the sabkha, Trucial Coast, Arabian Gulf. *J. Sediment. Res.*, **39**, 70–89.

Casas, E. and **Lowenstein, T.K.** (1989) Diagenesis of saline pan halite; comparison of petrographic features of modern, Quaternary and Permian halites. *J. Sediment. Res.*, **59**, 724–739.

Dellwig, L.F. (1955) Origin of the Salina salt of Michigan. *J. Sediment. Res.*, **25**, 83–110.

Eyal, H., **Enzel, Y.**, **Meiburg, E.**, **Vowinckel, B.** and **Lensky, N.G.** (2021) How does coastal gravel get sorted under stormy longshore transport? *Geophys. Res. Lett.*, **48**, e2021GL095082.

Eyal, H., **Armon, M.**, **Enzel, Y.** and **Lensky, N.G.** (2023) Synoptic-scale to mesoscale atmospheric circulation connects fluvial and coastal gravel conveyors and directional deposition of coastal landforms in the Dead Sea basin. *Earth Surface Dynamics*, **11**(4), 547–574.

Ezraty, R., **Mor, Z.**, **Bodzin, R.**, **Assouline, S.**, **Tanny, J.**, **Fratini, G.**, **Griessbaum, F.** and **Lensky, N.G.** (2021) Lorentzian filter correction of turbulence measurements on oscillating floating platforms: impact on wind spectra and eddy-covariance fluxes. *Water Resour. Res.*, **57**, e2020WR027583.

Flecker, R., **Krijgsman, W.**, **Capella, W.**, **de Castro Martíns, C.**, **Dmitrieva, E.**, **Mayser, J.P.**, **Marzocchi, A.**, **Modestou, S.**, **Ochoa, D.** and **Simon, D.** (2015) Evolution of the Late Miocene Mediterranean–Atlantic gateways and their impact on regional and global environmental change. *Earth-Sci. Rev.*, **150**, 365–392.

Fong, D.A. (1998) Dynamics of freshwater plumes: observations and numerical modeling of the wind-forced response and alongshore freshwater transport. Diss. Massachusetts Institute of Technology, 1998.

Fong, D.A. and **Geyer, W.R.** (2001) Response of a river plume during an upwelling favorable wind event. *J. Geophys. Res. Ocean.*, **106**, 1067–1084.

García-Veigas, J., **Cendón, D.I.**, **Rosell, L.**, **Ortí, F.**, **Ruiz, J.T.**, **Martín, J.M.** and **Sanz, E.** (2013) Salt deposition and brine evolution in the Granada Basin (Late Tortonian, SE Spain). *Palaeogeogr. Palaeoclimatol. Palaeoecol.*, **369**, 452–465.

Garfunkel, Z. (1981) Internal structure of the Dead Sea leaky transform (rift) in relation to plate kinematics. *Tectonophysics*, **80**, 81–108.

Gavrieli, I. (1997) Halite Deposition From the Dead Sea: 1960–1993. In: *The Dead Sea: The Lake and its Settings* (Eds Niemi, T.M., Ben-Avraham, Z. and Gat, J.R.), pp. 161–170. Oxford University Press, Oxford.

Gertman, I. and **Hecht, A.** (2002) The Dead Sea hydrography from 1992 to 2000. *J. Mar. Syst.*, **35**, 169–181.

Goodall, T.M., **North, C.P.** and **Glennie, K.W.** (2000) Surface and subsurface sedimentary structures produced by salt crusts. *Sedimentology*, **47**, 99–118.

Gvirtzman, Z., **Manzi, V.**, **Calvo, R.**, **Gavrieli, I.**, **Gennari, R.**, **Lugli, S.**, **Reghizzi, M.** and **Roveri, M.** (2017) Intra-Messinian truncation surface in the Levant Basin explained by subaqueous dissolution. *Geology*, **45**, 915–918.

Hamdani, I., **Assouline, S.**, **Tanny, J.**, **Lensky, I.M.**, **Gertman, I.**, **Mor, Z.** and **Lensky, N.G.** (2018) Seasonal and diurnal evaporation from a deep hypersaline lake: the Dead Sea as a case study. *J. Hydrol.*, **562**, 155–167.

Hetland, R.D. (2005) Relating river plume structure to vertical mixing. *J. Phys. Oceanogr.*, **35**, 1667–1688.

Hetland, R.D. (2010) The effects of mixing and spreading on density in near-field river plumes. *Dyn. Atmos. Oceans*, **49**, 37–53.

Hetland, R.D. and **Hsu, T.J.** (2013) Freshwater and sediment dispersal in large river plumes. *Biogeochem. Dyn. Large River-Coastal Interfaces Linkages with Glob. Clim. Chang. Ed. by Bianchi, TS, Allison, MA, Cai, W.-J., Springer, New York, USA*, 55–85.

Horner-Devine, A.R., **Hetland, R.D.** and **MacDonald, D.G.** (2015) Mixing and transport in coastal river plumes. *Annu. Rev. Fluid Mech.*, **47**, 569–594.

Hovorka, S. (1987) Depositional environments of marine-dominated bedded halite, Permian San Andres Formation, Texas. *Sedimentology*, **34**, 1029–1054.

Hovorka, S.D., **Holt, R.M.** and **Powers, D.W.** (2007) Depth indicators in Permian Basin evaporites. *Geol. Soc. London Spec. Publ.*, **285**, 335–364.

Israel Hydrological Service (2024) *Dead Sea Level Data 1976–2024*. Jerusalem, Israel.

Jagniecki, E.A. and **Lowenstein, T.K.** (2015) Evaporites of the Green River Formation, Bridger and Piceance Creek Basins: deposition, diagenesis, paleobrine chemistry, and Eocene atmospheric CO_2. Stratigr. Paleolimnol. Green River Form. West. USA, 277–312.

Jarvis, R.A. and **Woods, A.W.** (1994) The nucleation, growth and settling of crystals from a turbulently convecting fluid. *J. Fluid Mech.*, **273**, 83–107.

Kahana, R., **Ziv, B.**, **Enzel, Y.** and **Dayan, U.** (2002) Synoptic climatology of major floods in the Negev Desert, Israel. *Int. J. Climatol.*, **22**, 867–882.

Karakitsios, V., **Cornée, J.-J.**, **Tsourou, T.**, **Moissette, P.**, **Kontakiotis, G.**, **Agiadi, K.**, **Manoutsoglou, E.**, **Triantaphyllou, M.**, **Koskeridou, E.** and **Drinia, H.** (2017) Messinian salinity crisis record under strong freshwater input in marginal, intermediate, and deep environments: The case of the North Aegean. *Palaeogeogr. Palaeoclimatol. Palaeoecol.*, **485**, 316–335.

Kirkland, D.W., **Denison, R.E.** and **Dean, W.E.** (2000) Parent brine of the castile evaporites (Upper Permian), Texas and New Mexico. *J. Sediment. Res.*, **70**, 749–761.

Kiro, Y., **Goldstein, S.L.**, **Lazar, B.** and **Stein, M.** (2016) Environmental implications of salt facies in the Dead Sea. *Geol. Soc. Am. Bull.*, **128**, 824–841.

Kiro, Y., **Goldstein, S.L.**, **Garcia-Veigas, J.**, **Levy, E.**, **Kushnir, Y.**, **Stein, M.** and **Lazar, B.** (2017) Relationships between lake-level changes and water and salt budgets in the Dead Sea during extreme aridities in the Eastern Mediterranean. *Earth Planet. Sci. Lett.*, **464**, 211–226.

Krijgsman, W. and **Meijer, P.T.** (2008) Depositional environments of the Mediterranean "Lower Evaporites" of the Messinian salinity crisis: Constraints from quantitative analyses. *Mar. Geol.*, **253**, 73–81.

Lensky, N. and **Dente, E.** (2015) The hydrological proecesses driving the accelerated Dead Sea level decline in the past decades. Geological Survey of Israel Report. *GSI/16/2015*, 22 pp.

Lensky, N.G., **Dvorkin, Y.**, **Lyakhovsky, V.**, **Gertman, I.** and **Gavrieli, I.** (2005) Water, salt, and energy balances of the Dead Sea. *Water Resour. Res.*, **41**, 1–13.

Lensky, N.G., **Lensky, I.M.M.**, **Peretz, A.**, **Gertman, I.**, **Tanny, J.** and **Assouline, S.** (2018) Diurnal course of evaporation from the Dead Sea in summer: a distinct double peak induced by solar radiation and night sea breeze. *Water Resour. Res.*, **54**, 150–160.

Levy, Y. (1992) *Modern Sedimentation in the Dead Sea (1982–1989)*. Geological Survey of Israel, TR-GSI/7, Jerusalem. 92.

Li, J., **Lowenstein, T.K.**, **Brown, C.B.**, **Ku, T.-L.** and **Luo, S.** (1996) A 100 ka record of water tables and paleoclimates from salt cores, Death Valley, California. *Palaeogeogr. Palaeoclimatol. Palaeoecol.*, **123**, 179–203.

Lokier, S.W. (2012) Development and evolution of subaerial halite crust morphologies in a coastal sabkha setting. *J. Arid Environ.*, **79**, 32–47.

Lowenstein, T.K. (1988) Origin of depositional cycles in a Permian "saline giant": The Salado (McNutt zone) evaporites of New Mexico and Texas. *Bull. Geol. Soc. Am.*, **100**, 592–608.

Lowenstein, T.K. and **Hardie, L.A.** (1985) Criteria for the recognition of salt-pan evaporites. *Sedimentology*, **32**, 627–644.

Manzi, V., **Gennari, R.**, **Lugli, S.**, **Roveri, M.**, **Scafetta, N.** and **Schreiber, B.C.** (2012) High-frequency cyclicity in the Mediterranean Messinian evaporites: evidence for Solar-Lunar climate forcing. *J. Sediment. Res.*, **82**, 991–1005.

Mor, Z., **Assouline, S.**, **Tanny, J.**, **Lensky, I.M.** and **Lensky, N.G.** (2018) Effect of water surface salinity on evaporation: the case of a diluted buoyant plume over the Dead Sea. *Water Resour. Res.*, **54**, 1460–1475.

Mor, Z., **Lutzky, H.**, **Shalev, E.** and **Lensky, N.G.** (2021) Hydrostatic densitometer for monitoring density in freshwater to hypersaline water bodies. *Water*, **13**, 1842.

Morris, R.C. and **Dickey, P.A.** (1957) Modern evaporite deposition in Peru. *Am. Assoc. Pet. Geol. Bull.*, **41**, 2467–2474.

Olson, K.J. and **Lowenstein, T.K.** (2021) Searles Lake evaporite sequences: Indicators of late Pleistocene/Holocene lake temperatures, brine evolution, and p CO_2. *Bulletin*, **133**, 2319–2334.

Olson, K.J., **Demicco, R.V.** and **Lowenstein, T.K.** (2023) Seasonal dynamics of evaporite mineral precipitation, dissolution, and back-reactions in shallow and deep hypersaline lakes. *Geochim. Cosmochim. Acta*, **351**, 51–65.

Ouillon, R., **Lensky, N.G.**, **Lyakhovsky, V.**, **Arnon, A.** and **Meiburg, E.** (2019) Halite precipitation from double-diffusive salt fingers in the dead sea: numerical simulations. *Water Resour. Res.*, **55**, 4252–4265.

Palchan, D., **Neugebauer, I.**, **Amitai, Y.**, **Waldmann, N.D.**, **Schwab, M.J.**, **Dulski, P.**, **Brauer, A.**, **Stein, M.**, **Erel, Y.** and **Enzel, Y.** (2017) North Atlantic controlled depositional cycles in MIS 5e layered sediments from the deep Dead Sea basin. *Quat. Res.*, **87**, 168–179.

Roberts, S.M. and **Spencer, R.J.** (1995) Paleotemperatures preserved in fluid inclusions in halite. *Geochim. Cosmochim. Acta*, **59**, 3929–3942.

Roedder, E. (1982) Possible Permian diurnal periodicity in NaCl precipitation, Palo Duro Basin, Texas. Geol. Geohydrology Palo Duro Basin, Texas Panhand. Bur. Econ. Geol. Univ. Texas Austin, Geol. Circ., 82–87.

Roveri, M., **Flecker, R.**, **Krijgsman, W.**, **Lofi, J.**, **Lugli, S.**, **Manzi, V.**, **Sierro, F.J.**, **Bertini, A.**, **Camerlenghi, A.**, **De Lange, G.**, **Govers, R.**, **Hilgen, F.J.**, **Hübscher, C.**, **Meijer, P.T.** and **Stoica, M.** (2014a) The Messinian Salinity Crisis: past and future of a great challenge for marine sciences. *Mar. Geol.*, **352**, 25–58.

Roveri, M., **Manzi, V.**, **Bergamasco, A.**, **Falcieri, F.M.**, **Gennari, R.**, **Lugli, S.** and **Schreiber, B.C.** (2014b) Dense shelf water cascading and messinian canyons: a new scenario for the mediterranean salinity crisis. *Am. J. Sci.*, **314**, 751–784.

Sade, A.R., **Hall, J.K.**, **Sade, H.**, **Amit, G.**, **Tibor, G.**, **Schulze, B.**, **Gur-Arieh, I.**, **ten Brink, U.**, **Ben Avraham, Z.**, **Keller, C.**, **Gertman, I.**, **Beaudoin, J.**, **Al-Zoubi, A.S.**, **Akawwi, E.**, **Rimawi, O.**, **Abueladas, A.**, **Mayer, L.A.**, **Calder, B.R.** and **Maratos, A.** (2014) Multibeam Bathymetric Map of the Dead Sea. Jerusalem, GSI/01/2014.

Schmalz, R.F. (1969) deep-water evaporite deposition: a genetic model. *Am. Assoc. Pet. Geol. Bull.*, **53**, 798–823.

Schubel, K.A. and **Lowenstein, T.K.** (1997) Criteria for the recognition of shallow-perennial-saline-lake halites based on recent sediments from the Qaidam Basin, western China. *J. Sediment. Res.*, **67**, 74–87.

Sirota, I., **Arnon, A.** and **Lensky, N.G.** (2016) Seasonal variations of halite saturation in the Dead Sea. *Water Resour. Res.*, **52**, 7151–7162.

Sirota, I., **Enzel, Y.** and **Lensky, N.G.** (2017) Temperature seasonality control on modern halite layers in the Dead Sea: in situ observations. *Bull. Geol. Soc. Am.*, **129**, 1181–1194.

Sirota, I., **Enzel, Y.** and **Lensky, N.G.** (2018) Halite focusing and amplification of salt layer thickness: from the Dead Sea to deep hypersaline basins. *Geology*, **46**, 851–854.

Sirota, I., **Ouillon, R.**, **Mor, Z.**, **Meiburg, E.**, **Enzel, Y.**, **Arnon, A.** and **Lensky, N.G.** (2020) Hydroclimatic controls on salt fluxes and halite deposition in the dead sea and the shaping of "Salt Giants". *Geophys. Res. Lett.*, **47**, e2020GL090836.

Sirota, I., **Enzel, Y.**, **Mor, Z.**, **Ben Moshe, L.**, **Eyal, H.**, **Lowenstein, T.K.** and **Lensky, N.G.** (2021) Sedimentology and stratigraphy of a modern halite sequence formed under Dead Sea level fall. *Sedimentology*, **68**, 1069–1090.

Steinhorn, I. (1983) In situ salt precipitation at the Dead Sea. *Limnol. Oceanogr.*, **28**, 580–583.

Steinhorn, I. (1985) The disappearance of the long term meromictic stratification of the Dead Sea. *Limnol. Oceanogr.*, **30**, 451–472.

Stiller, M., **Gat, J.R.** and **Kaushansky, P.** (1997) Halite precipitation and sediment deposition as measured in sediment traps deployed in the Dead Sea: 1981–1983. In: *The Dead Sea: The Lake and Its Settings* (Eds Niemi, T.M., Ben-Avraham, Z. and Gat, J.R.), pp. 161–170. Oxford University Press, Oxford.

Tau, G., **Enzel, Y.**, **McGowan, H.**, **Lyakhovsky, V.** and **Lensky, N.G.** (2022) Air-water interactions regulating water temperature of lakes: direct observations (Agamon Hula, Israel) and analytical solutions. *J. Hydrol.*, **614**, 128515.

Torfstein, A., **Goldstein, S.L.**, **Kushnir, Y.**, **Enzel, Y.**, **Haug, G.** and **Stein, M.** (2015) Dead Sea drawdown and monsoonal impacts in the Levant during the last interglacial. *Earth Planet. Sci. Lett.*, **412**, 235–244.

Warren, J.K. (2010) Evaporites through time: tectonic, climatic and eustatic controls in marine and nonmarine deposits. *Earth-Sci. Rev.*, **98**, 217–268.

Yoshimura, T., **Kuroda, J.**, **Lugli, S.**, **Tamenori, Y.**, **Ogawa, N.O.**, **Jimenez-Espejo, F.J.**, **Isaji, Y.**, **Roveri, M.**, **Manzi, V.**, **Kawahata, H.** and **Ohkouchi, N.** (2016) An X-ray spectroscopic perspective on Messinian evaporite from Sicily: sedimentary fabrics, element distributions, and chemical environments of S and Mg. *Geochem. Geophys. Geosyst.*, **17**, 1383–1400.

Manuscript received 11 July 2023; revision accepted 3 June 2024

Supporting Information

Additional information may be found in the online version of this article:

Appendix S1. The cumulates crystal size.

Appendix S2. Comparison of evaporation in the two studied environments.

Appendix S3. Weekly measurements of halite accumulation.

Figure S1. Halite crystal measurements.

Figure S2. Evaporation course in the two environments along the entire observation periods in winter 2021–2022.

Figure S3. Halite accumulation thickness on the concrete block at a water depth of 25 m, as observed by remotely operated vehicle (ROV).